



An adaptive strategy for discontinuous Galerkin simulations of Richards' equation

Jean-Baptiste Clément, Frederic Golay, Mehmet Ersoy, Damien Sous

► To cite this version:

Jean-Baptiste Clément, Frederic Golay, Mehmet Ersoy, Damien Sous. An adaptive strategy for discontinuous Galerkin simulations of Richards' equation. 2021. hal-03132113v1

HAL Id: hal-03132113

<https://hal.science/hal-03132113v1>

Preprint submitted on 4 Feb 2021 (v1), last revised 24 Mar 2021 (v2)

HAL is a multi-disciplinary open access archive for the deposit and dissemination of scientific research documents, whether they are published or not. The documents may come from teaching and research institutions in France or abroad, or from public or private research centers.

L'archive ouverte pluridisciplinaire **HAL**, est destinée au dépôt et à la diffusion de documents scientifiques de niveau recherche, publiés ou non, émanant des établissements d'enseignement et de recherche français ou étrangers, des laboratoires publics ou privés.

An adaptive strategy for discontinuous Galerkin simulations of Richards' equation

Jean-Baptiste Clément ^{1,2}, Frédéric Golay ^{1,*}, Mehmet Ersoy ¹, Damien Sous ^{2,3}

20th October 2020

¹ IMATH, EA 2134, Université de Toulon, CS 60584, 83041 Toulon Cedex 9, France

² Université de Toulon, Aix Marseille Université, CNRS, IRD, Mediterranean Institute of Oceanography (MIO), La Garde, France

³ Univ. Pau & Pays Adour / E2S UPPA, Laboratoire des Sciences de l'Ingénieur Appliquées à la Mécanique et au Génie Electrique (SIAME) - MIRA, EA4581, 64600, Anglet, France

Abstract

Numerical solution of Richards' equation remains challenging to get robust, accurate and cost-effective results, particularly for moving sharp wetting fronts. An adaptive strategy for both space and time is proposed to deal with 2D sharp wetting fronts associated with varying and possibly vanishing diffusivity caused by nonlinearity, heterogeneity and anisotropy. Adaptive time stepping makes nonlinear convergence reliable and backward difference formula provides high-order time scheme. Adaptive mesh refinement tracks wetting fronts with an *a posteriori* error indicator. The novelty of this paper consists in using this technique in combination with a weighted discontinuous Galerkin framework to better approximate steep wetting fronts by a discontinuity. The potential of the overall approach is shown through various examples including analytical and laboratory benchmarks and simulation of full-scale multi-materials dam wetting experiment.

Keywords: Unsaturated porous media, Weighted Discontinuous Galerkin method, Adaptive Mesh Refinement, *A posteriori* error estimation, Adaptive time stepping, BDF.

1 Introduction

Predicting variably-saturated flows in porous media is a major issue for many fields in science and engineering. For example, such flows arise in soil physics, hydrogeology, environment, agriculture or oil industry for problems like subsurface contaminant transport, petroleum reservoir, water resources, surface ponding, *etc.*

In the present work, flows in variably-saturated porous media are described by Richards' equation. What makes Richards' equation very attractive is that it models the porous medium as a whole part including both saturated and unsaturated zones. Richards' equation is a nonlinear parabolic equation which can degenerate into an elliptic equation under complete saturation

* Corresponding author.

Email addresses: jean-baptiste.clement@univ-tln.fr (J.-B. Clément), frederic.golay@univ-tln.fr (F. Golay), mehmet.ersoy@univ-tln.fr (M. Ersoy), damien.sous@mio.osupytheas.fr (D. Sous).

condition. Richards' equation has been extensively used for numerical simulations by the hydrogeology community, see *e.g.* [47, 46]. Despite this research effort, many numerical challenges remain for solving Richards' equation with some simulations being still unreliable and/or expensive [18, 57]. This numerical complexity prevented a more general use of Richards based model for a number of applications. Indeed, the solution of Richards' equation involves sharp wetting fronts which evolve both in space and time and are difficult to resolve. Besides, the simulation must treat simultaneously unsaturated/saturated regions of parabolic/elliptic natures, several porous media of different hydraulic properties and possibly fast-changing boundary conditions. These aspects can also lead to steep gradients acting like discontinuities. Considering the set of nonlinear functions for hydraulic properties, it is seldom possible to foresee the behaviour of Richards' equation and getting numerical solutions can be hard to achieve. Especially, numerical schemes often fail to converge or need fine discretization, making computation costly.

In this paper, a discontinuous Galerkin (DG) method is chosen to solve Richards' equation. DG methods are based on a variational formulation in an element-wise fashion, sharing advantages both with finite elements and finite volumes methods. In particular, they are locally conservative which is crucial in fluid dynamics [39]. Moreover, the nature of DG formulation enables to work on non-conforming mesh and to change locally the degree of polynomial approximation. This is an important benefit since adaptive mesh refinement (AMR), the so-called h -adaptation, and high-order accuracy, the so-called p -adaptation, become possible [11], promoting a growing use of DG methods for transport phenomena in porous media such as two-phase flow problems [24, 2]. However, DG methods remain sparsely applied to Richards' equation. In 2007, Li *et al.* solved Richards' equation in 1D with a local discontinuous Galerkin method [27, 26]. Sochala discretized Richards' equation through a SIPG mixed DG formulation in 2008 [44, 43]. Recently, in 2019, Dolejší *et al.* proposed a space-time DG method for solving Richards' equation [12].

To reach robustness and accuracy, an adaptive strategy is developed in this paper. Richards' equation is known to be a stiff differential equation with difficult convergence [35, 25, 28] so the time discretization and the nonlinear solver have to be addressed carefully. Adaptive mesh refinement will be used to capture moving wetting fronts thanks to *a posteriori* estimation. h -Adaptation is employed for two-phase flow in porous media [24] but also for Richards' equation [32, 26]. Making the most of DG methods flexibility, adaptive mesh refinement is combined with a weighted discontinuous Galerkin (WDG) framework which allows discontinuity in the solution according to the nonlinear diffusivity. Following earlier works, this approach was formulated by Ern, Di Pietro and other collaborators [15, 10] and by Proft and Rivière under the name *improved* and *adapted* discontinuous Galerkin methods [37, 38]. Application of such strategy for Richards' equation, combining adaptive mesh refinement, *a posteriori* estimation and WDG framework, is the main novelty of the present study.

The Richards' equation framework is first recalled in Section 2. In Section 3, Richards' equation discretization is presented through a DG framework and then solved by a nonlinear iterative process aiming to robustness. Section 4 is dedicated to the adaptive strategy proposed to improve solving of Richards' equation. Several numerical experiments are discussed in Section 5. In particular, the modeling strategy is tested on a challenging benchmark case of full-scale wetting of a multi-materials dam. Finally, Section 6 is devoted to some concluding remarks.

2 Model problem

2.1 Richards' equation

Richards' equation is a classical nonlinear parabolic equation used to describe flow in unsaturated/saturated zones of an aquifer. Derivation of Richards' equation is described for instance in [46]. Variables in play are θ the water content [-], ψ the pressure head [L] and \mathbb{K} the hydraulic conductivity tensor [L · T⁻¹]. The mixed formulation is selected in the present study owing to its versatility [18]:

$$\partial_t \theta(\psi) - \nabla \cdot (\mathbb{K}(\psi) \nabla (\psi + z)) = 0. \quad (1)$$

Alternative pressure-based or saturation-based formulations have been discarded because they are either non-conservative or undefined for complete saturation and heterogeneous soils [7]. The mixed formulation can be rewritten in the hydraulic head form which is more common in hydrology:

$$\partial_t \theta(h - z) - \nabla \cdot (\mathbb{K}(h - z) \nabla h) = 0, \quad (2)$$

55 where $h = \psi + z$ is the hydraulic head [L]. One can also add a source/sink term Q [T⁻¹] to Richards' equation to model various processes, like bacteria colony or plant roots, or to couple Richards' equation with free surface flow.

Solving Eq. (1) requires two constitutive laws: one for hydraulic conductivity and one for water content. Several models have been proposed, depending on the hydraulic properties of
60 the porous medium.

The hydraulic conductivity \mathbb{K} is generally supposed to react to saturation identically for each space direction. This leads to write:

$$\mathbb{K}(\psi) = \mathbb{K}_s K_r(\psi), \quad (3)$$

where \mathbb{K}_s the intrinsic or saturated hydraulic conductivity tensor [L · T⁻¹] and K_r the relative hydraulic conductivity [-].

For practical purposes, the water content is often described in terms of effective saturation S_e [-]:

$$S_e(\psi) = \frac{\theta(\psi) - \theta_r}{\theta_s - \theta_r}, \quad (4)$$

where θ_s denotes the saturated water content [-] and θ_r the residual water content [-], corresponding to the maximal and minimal saturations, respectively.

The hydraulic properties present two different behaviours depending on whether the porous media is saturated ($\psi \geq 0$) or not ($\psi < 0$):

$$S_e(\psi) = \begin{cases} 1 & \text{if } \psi \geq 0, \\ S_e & \text{otherwise,} \end{cases} \quad \text{and} \quad K_r(\psi) = \begin{cases} 1 & \text{if } \psi \geq 0, \\ K_r & \text{otherwise.} \end{cases} \quad (5)$$

65 S_e and K_r are monotonic increasing functions of pressure head ψ in the unsaturated zone. The water table corresponds to $\psi = 0$ by definition and is considered belonging to the saturated zone. The capillary fringe is the layer above water table where water is raised due to capillary actions. It belongs to the unsaturated zone and there is no standard definition for its upper limit. Throughout this paper, several constitutive laws will be used to model hydraulic properties in
70 the unsaturated zone. They are compiled in Tab. 1.

Name	Expression	Parameters
Gardner-Irmy relations (1958) [23, 21]	$S_e = e^{\frac{\alpha\psi}{m}}$ $K_r = e^{\alpha\psi} \frac{C}{C + \psi ^D}$	α : pore-size distribution [-] m : tortuosity [-]
Vachaud's relations (1971) [51]	$S_e = \frac{C}{C + \psi ^D}$ $K_r = \frac{A}{A + \psi ^B}$	A, C : empirical shape parameters [$L^{B;D}$] B, D : empirical shape parameters [-]
Van Genuchten-Mualem relations (1980) [34, 52]	$S_e = (1 + (\alpha \psi ^n)^{-m})^{-\frac{1}{m-1}}$ $K_r = S_e^l \left(1 - \left(1 - S_e^{\frac{1}{m}}\right)^m\right)^2$	$l = \begin{cases} 0.5 & \text{for Mualem [34]} \\ 1 & \text{for Burdine [5]} \end{cases}$: pore connectivity [-] α : parameter linked to air entry pressure inverse [L^{-1}] $n > 1$: pore-size distribution [-] $m = 1 - \frac{1}{n}$: pore-size distribution [-]

Table 1: Hydraulic relations used in this paper.

It is worth noting that:

- under complete saturation, hydraulic properties become constant and Richards' equation degenerates into an elliptic equation characterised by fast diffusion;
- under almost complete unsaturation, hydraulic properties get very near-zero values which stop diffusion and may be inconvenient numerically;
- for particular set of parameters, when $\psi \rightarrow 0^-$, constitutive laws may exhibit very steep gradients.

These constitutive laws are mainly responsible for the numerical challenges of Richards' equation, such as nonlinearities, degeneracies and instabilities, which are often observed in the presence of material heterogeneities or dynamic boundary conditions like seepage boundary condition.

2.2 Seepage boundary condition

The seepage boundary condition is specific to subsurface model [41]. This condition is used to model the interface between a porous medium and the atmosphere. If the porous medium is saturated and an outflow occurs, then water pours out at atmospheric pressure: $\psi = 0 \iff h = z$. Otherwise, the interface acts as an impervious boundary and there is no flux. This condition mimics an outflow condition. Figure 1 depicts the situation. The treatment of the seepage boundary condition is difficult because the length of seepage face is unknown *a priori*: it depends on the sought solution.

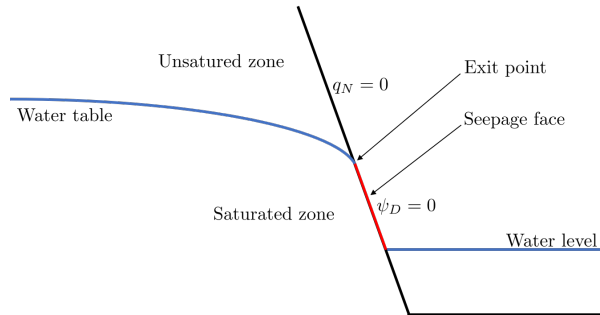


Figure 1: Seepage modelling by the boundary condition.

There are many ways to numerically express the seepage boundary condition: condition of Signorini's type [43], variational inequality, etc. A simple approach is to consider a switch between a Dirichlet and a Neumann boundary condition:

$$\begin{cases} h = z & \text{if } h \geq z \text{ and } -\mathbb{K}(h - z)\nabla h \cdot \mathbf{n} > 0, \\ -\mathbb{K}(h - z)\nabla h \cdot \mathbf{n} = 0 & \text{otherwise.} \end{cases} \quad (6)$$

Alternatively, the seepage boundary condition may be interpreted as a nonlinear Robin boundary condition:

$$\mathbb{1}_S(h)(h - z) - (1 - \mathbb{1}_S(h))\mathbb{K}(h - z)\nabla h \cdot \mathbf{n} = 0, \quad (7)$$

where the seepage indicator function is:

$$\mathbb{1}_S: \Gamma_S \rightarrow \{0, 1\} \quad (8)$$

$$h \mapsto \begin{cases} 1 & \text{if } h \geq z \text{ and } -\mathbb{K}(h - z)\nabla h \cdot \mathbf{n} > 0, \\ 0 & \text{otherwise.} \end{cases} \quad (9)$$

90 This compact formulation will be used here, keeping in mind that it encompasses a mix of a Dirichlet and a Neumann boundary conditions such as in Eq. (6).

3 Numerical methods

3.1 Discontinuous Galerkin discretization

95 More careful developments about discontinuous Galerkin (DG) methods can be found in Rivière [39] or Dolejší and Feistauer [11]. Let $d \in \{1, 2, 3\}$ be the dimension. The porous medium is represented by the computational domain $\Omega \subset \mathbb{R}^d$ of boundary $\partial\Omega$ and the final time is $T \in \mathbb{R}_+^*$. The boundary $\partial\Omega$ is subdivided into three mutually disjoint boundaries, $\partial\Omega = \Gamma_D \cup \Gamma_N \cup \Gamma_S$, corresponding to the Dirichlet, Neumann and seepage boundary conditions respectively. The following problem is considered:

$$\begin{aligned} & \text{find } h(\mathbf{x}, t) : \Omega \times (0, T) \longrightarrow \mathbb{R} \text{ such that} \\ & \begin{cases} \partial_t \theta(h - z) - \nabla \cdot (\mathbb{K}(h - z)\nabla h) = 0, & \text{in } \Omega \times (0, T), \\ h = h_0, & \text{in } \Omega \times \{0\}, \\ h = h_D, & \text{on } \Gamma_D \times (0, T), \\ -\mathbb{K}(h - z)\nabla h \cdot \mathbf{n} = q_N, & \text{on } \Gamma_N \times (0, T), \\ \mathbb{1}_S(h)(h - z) - (1 - \mathbb{1}_S(h))\mathbb{K}(h - z)\nabla h \cdot \mathbf{n} = 0, & \text{on } \Gamma_S \times (0, T). \end{cases} \end{aligned} \quad (10)$$

100 The time duration $(0, T)$ is subdivided into N time intervals such that $0 = t^0 < t^1 < \dots < t^N = T$. Let $n \in \mathbb{N}, 0 < n \leq N$: if the time interval $T^n = [t^{n-1}, t^n]$ is considered, the corresponding time step is $\tau^n = t^n - t^{n-1}$.

Ω is subdivided into N_E mutually disjoint polygonal elements E forming a mesh. The mesh at the time partition T^n is denoted by $\mathcal{E}_h^n = \{E\}_{E \in \Omega}$. So, $\bar{\Omega} = \bigcup_{E \in \mathcal{E}_h^n} E$. Moreover, the boundary of one element $E \in \mathcal{E}_h^n$ is ∂E while its diameter h_E is defined by:

$$h_E := \sup_{\mathbf{x}, \mathbf{y} \in E} |\mathbf{x} - \mathbf{y}|. \quad (11)$$

For every mesh \mathcal{E}_h^n , the space step is set as:

$$h^n := \max_{E \in \mathcal{E}_h^n} (h_E). \quad (12)$$

The set of all open faces of all elements $E \in \mathcal{E}_h^n$ is denoted by \mathcal{F}_h^n . Furthermore, these definitions stand:

$$\mathcal{F}_{h,D}^n := \bigcup_{F \in \Gamma_D} F, \quad \mathcal{F}_{h,N}^n := \bigcup_{F \in \Gamma_N} F, \quad \mathcal{F}_{h,S}^n := \bigcup_{F \in \Gamma_S} F \quad (13)$$

$$\mathcal{F}_{h,B}^n := \mathcal{F}_{h,D}^n \cup \mathcal{F}_{h,N}^n \cup \mathcal{F}_{h,S}^n, \quad \mathcal{F}_{h,I}^n := \mathcal{F}_h^n \setminus \mathcal{F}_{h,B}^n. \quad (14)$$

For each face $F \in \mathcal{F}_h^n$, there is a unit normal vector \mathbf{n}_F . For $F \in \mathcal{F}_{h,I}^n$, its orientation is arbitrary but kept fixed and, for $F \in \mathcal{F}_{h,B}^n$, it is oriented outward.

Let two neighbouring elements E_l and E_r sharing one face $F \in \mathcal{F}_{h,I}^n$. There are two traces of a function u along F denoted by u_l and u_r :

$$\mathbf{x} \in F, u_l(\mathbf{x}) := \lim_{\varepsilon \rightarrow 0^+} u(\mathbf{x} + \varepsilon \mathbf{n}_F), \quad \mathbf{x} \in F, u_r(\mathbf{x}) := \lim_{\varepsilon \rightarrow 0^-} u(\mathbf{x} + \varepsilon \mathbf{n}_F). \quad (15)$$

Formally, the jump and the mean of the function u across a face $F \in \mathcal{F}_{h,I}^n$ are defined respectively by:

$$\llbracket u \rrbracket := u_l - u_r, \quad \{u\} := \frac{1}{2}(u_l + u_r). \quad (16)$$

In the case that $F \in \mathcal{F}_{h,B}^n$, $\llbracket u \rrbracket = \{u\} = u_l$ where u_l is the trace of the function u from the element which holds F . Throughout this paper, the quantity h_F denotes the length of $F \in \mathcal{F}_h^n$ and p_F the mean of polynomial degree of neighbouring elements:

$$h_F := |F|, \quad p_F := \sqrt{\llbracket p^2 \rrbracket}. \quad (17)$$

In the following derivation of the DG variational formulation, several interior penalty methods are considered. Their numerical properties are slightly different. Further information are available in [39, 11] for example. They use discontinuous approximations over the mesh \mathcal{E}_h^n defining a so-called broken Sobolev space $H^s(\mathcal{E}_h^n)$ with $s > 3/2$. The solution is sought in a subspace of this broken Sobolev space, taken to be:

$$S_p(\mathcal{E}_h^n) := \{v \in L^2(\Omega) : v|_E \in \mathbb{P}_p(E), \forall E \in \mathcal{E}_h^n\}, \quad (18)$$

105 where $\mathbb{P}_p(E)$ denotes the space of polynomial functions on E of degree less than $p \in \mathbb{N}$.

Equation (10) is multiplied by a test function $v \in S_p(\mathcal{E}_h^n)$ and then integrated on each element $E \in \mathcal{E}_h^n$. Green's theorem is used element-wise before summing over all elements in \mathcal{E}_h^n . The Neumann boundary condition has appeared naturally within the formulation and has been substituted. So it stands for the homogeneous Neumann part of the seepage boundary condition.

110 On one hand, knowing $\forall u, v \in S_p(\mathcal{E}_h^n)$, $\llbracket uv \rrbracket = \{u\} \llbracket v \rrbracket + \{v\} \llbracket u \rrbracket$ and assuming $\llbracket \mathbb{K}(h - z) \nabla h \cdot \mathbf{n}_F \rrbracket = 0$ because this quantity is smooth enough, product jump is decomposed and simplified where it is possible.

On the other hand, two penalty terms are considered. One mimics the solution continuity by constraining the interior solution jump to be zero, and one enforces the Dirichlet boundary condition, including the remaining part of the seepage boundary condition. If the solution is a continuous function satisfying the Dirichlet boundary conditions, the two penalty terms are vanishing so they can be added to the formulation:

$$J_I(h, v) = \sum_{F \in \mathcal{F}_h^I} \int_F \varrho_F^I \llbracket h \rrbracket \llbracket v \rrbracket dF, \quad J_D(h, v) = \sum_{F \in \mathcal{F}_h^D} \int_F \varrho_F^D h v dF. \quad (19)$$

The interior and Dirichlet penalty weights are set as:

$$\varrho_F^I = \frac{\sigma_F^I \gamma_F}{\mu_F} \quad \text{and} \quad \varrho_F^D = \frac{\sigma_F^D \gamma_F}{\mu_F}. \quad (20)$$

where the face measure is defined as $\mu_F = \frac{h_F}{p_F^2}$ and where σ_F^I , σ_F^D and γ_F are suitable chosen

115 positive constants. σ_F^I , σ_F^D are a user-defined parameter which must be above a threshold value to provide coercivity and guarantee stability for some of the DG methods [14]. γ is a diffusion penalty coefficient set to one generally whereas some studies consider other values, see *e.g.* [40].

A first weak formulation rises but it is not is not symmetric between the unknown h and the test function v . Making the formulation symmetrical can be useful to preserve the natural
120 symmetry in the discrete diffusion operator, to use appropriate solvers or to enhance numerical properties of the formulation. This can be done by adding the corresponding symmetric term which vanishes because $[[h]] = 0$ if h is a sufficiently smooth function.

Finally, the space semidiscretization reads:

$$\text{find } h \in S_p(\mathcal{E}_h^n) \text{ such that } \forall v \in S_p(\mathcal{E}_h^n), \quad m_{h,n}(\partial_t \theta(h - z), v) + a_{h,n}(h, v) = l_{h,n}(v), \quad (21)$$

where the DG bilinear forms, m and a , and linear form l are:

$$m_{h,n}(\partial_t \theta(h - z), v) = \sum_{E \in \mathcal{E}_h} \int_E \partial_t \theta(h - z) v \, dE, \quad (22)$$

$$\begin{aligned} a_{h,n}(h, v) = & \sum_{E \in \mathcal{E}_h} \int_E \mathbb{K}(h - z) \nabla h \cdot \nabla v \, dE - \sum_{F \in \mathcal{F}_h^I} \int_F [[\mathbb{K}(h - z) \nabla h \cdot \mathbf{n}_F]] [[v]] \, dF \\ & - \sum_{F \in \mathcal{F}_h^D} \int_F \mathbb{K}(h - z) \nabla h \cdot \mathbf{n}_F v \, dF + \sum_{F \in \mathcal{F}_h^D} \int_F \varrho_F^D h v \, dF - \sum_{F \in \mathcal{F}_h^S} \int_F \mathbb{1}_S(h) \mathbb{K}(h - z) \nabla h \cdot \mathbf{n}_F v \, dF \\ & + \sum_{F \in \mathcal{F}_h^I} \int_F \varrho_F^I [[h]] [[v]] \, dF + \sum_{F \in \mathcal{F}_h^S} \int_F \varrho_F^D \mathbb{1}_S(h) h v \, dF - \Theta \sum_{F \in \mathcal{F}_h^I} \int_F [[\mathbb{K}(h - z) \nabla v \cdot \mathbf{n}_F]] [[h]] \, dF \\ & - \Theta \sum_{F \in \mathcal{F}_h^D} \int_F \mathbb{K}(h - z) \nabla v \cdot \mathbf{n}_F h \, dF - \Theta \sum_{F \in \mathcal{F}_h^S} \int_F \mathbb{1}_S(h) \mathbb{K}(h - z) \nabla v \cdot \mathbf{n}_F h \, dF, \end{aligned} \quad (23)$$

$$\begin{aligned} l_{h,n}(v) = & \sum_{F \in \mathcal{F}_h^D} \int_F \varrho_F^D h_D v \, dF + \sum_{F \in \mathcal{F}_h^S} \int_F \varrho_F^D \mathbb{1}_S(h) z v \, dF - \sum_{F \in \mathcal{F}_h^N} \int_F q_N v \, dF \\ & - \Theta \sum_{F \in \mathcal{F}_h^D} \int_F \mathbb{K}(h - z) \nabla v \cdot \mathbf{n}_F h_D \, dF - \Theta \sum_{F \in \mathcal{F}_h^S} \int_F \mathbb{1}_S(h) \mathbb{K}(h - z) \nabla v \cdot \mathbf{n}_F z \, dF. \end{aligned} \quad (24)$$

$\Theta = \{-1, 0, 1\}$ is a constant leading to different symmetric versions of the DG formulation listed in Tab. 2.

Penalization		Symmetrization		
		$\Theta = -1$	$\Theta = 0$	$\Theta = 1$
	$\forall F \in \mathcal{F}_h, \sigma_F^I = \sigma_F^D = 0$	OBB method	-	global element method
	$\forall F \in \mathcal{F}_h, \sigma_F^I \neq 0, \sigma_F^D \neq 0$	NIPG	IIPG	SIPG

NIPG: non-symmetric interior penalty Galerkin

SIPG: symmetric interior penalty Galerkin

IIPG: incomplete interior penalty Galerkin

OBB method: Oden-Baumann-Babuška method

Table 2: Different types of DG methods.

125

The seepage boundary condition is treated numerically thanks to the indicator function $\mathbb{1}_S$ which alternates dynamically between the Dirichlet part when $\mathbb{1}_S = 1$ and the Neumann part for $\mathbb{1}_S = 0$, directly in the usual weak framework of the DG methods. This treatment can model any physical situations, like multiple seepage faces simultaneously, because it does not require any assumption about the mesh or seepage face [41].

130

3.2 Time discretization

To get the fully discrete DG formulation, the time derivative has now to be discretized. Such a procedure which takes care of space discretization before time discretization is called the method of lines. It is used commonly by others studies for Richards' equation, see *e.g.* [32, 27, 18].

Backward differentiation formula (BDF) are implicit numerical integration methods especially used for stiff differential equations thanks to their wide region of stability. These linear multistep methods use q already computed solutions to produce a method of order q . BDF with $q > 6$ are not stable. Analysis can be found in [42, 13]. The 1-step BDF is the backward Euler scheme. For this study, BDF are interesting because they provide high-order accuracy in time which is suitable if one wants to reach high-order in space without loss of gain. To initialize the scheme with q -step BDF, the first time step is subdivided into as many times as necessary to compute the sub-time steps with an increasing sequence of lower-order BDF. Even though the backward Euler scheme has error of order one in time, it will be particularly used for Richards' equation in this study because it provides good stability properties and remains simple. The following notation will be used for any function $u \in L^2(0, T; \Omega)$:

$$\forall n \in \mathbb{N}_+, u^n := u(\mathbf{x}, t_n). \quad (25)$$

The DG formulation in Eq. (21) is integrated over T^n and the time integral is approximated by the BDF methods of $0 < q < 7$ steps:

find a sequence of $(h^n)_{n \in \mathbb{N}_+} \in S_p(\mathcal{E}_h^n)$ such that

$$\begin{cases} h^0 = h_0, \\ \forall v \in S_p(\mathcal{E}_h^n), \quad m_{h,n} \left(\sum_{k=0}^q \frac{\alpha_{q,k}}{\tau^n} \theta(h^{n+1-k} - z), v \right) + a_{h,n}(h^{n+1}, v) = l_{h,n}(v, t^{n+1}), \end{cases} \quad (26)$$

where BDF coefficients are given in Tab. 3.

q	1	1	-1					
	2	3/2	-2	1/2				
	3	11/6	-3	3/2	-1/3			
	4	25/12	-4	3	-4/3	1/4		
	5	137/60	-5	5	-10/3	5/4	-1/5	
	6	49/20	-6	15/2	-20/3	15/4	-6/5	1/6
$\alpha_{s,k}$		0	1	2	3	4	5	6
		k						

Table 3: BDF coefficients $\alpha_{q,k}$ for all methods.

135

3.3 Linearization

Richards' equation is a nonlinear equation usually solved by an iterative procedure such as fixed-point iteration or Newton-Raphson method whose choice is determining for computation time

performances and convergence. Many studies have been carried out to compare these methods, and others, for solving Richards' equation for various problems[35, 25, 28]. They emphasize that fixed-point iteration and even Newton-Raphson scheme are very sensitive and do not converge systematically according to Richards' equation's formulations, initial and boundary conditions and because of the nonlinearities of constitutive laws. In particular, the nonlinear iterative solver can oscillate between two solutions. For this study, a damped Newton-Raphson method and a fixed-point method were implemented. Let m be the number of the nonlinear iteration. The residual of Eq. (26) is expressed as:

$$r_{h,n}(h^{n+1}, v) := m_{h,n} \left(\sum_{k=0}^q \frac{\alpha_{s,k}}{\tau^n} \theta(h^{n+1-k} - z), v \right) + a_{h,n}(h^{n+1}, v) - l_{h,n}(v; t^{n+1}). \quad (27)$$

The difference between two successive iterations is written $\delta_h^{n+1,m} := h^{n+1,m+1} - h^{n+1,m}$ so the iterative procedure reads:

$$\begin{cases} \frac{dr_{h,n}(h^{n+1,m}, v)}{dh^{n+1,m}} \delta_h^{n+1,m} = -r_{h,n}(h^{n+1,m}, v), \\ h^{n+1,m+1} = h^{n+1,m} + \delta_h^{n+1,m}. \end{cases} \quad (28)$$

Underlining ideas are already described in [25] and have just been adapted here to the DG system. Roughly speaking, a fixed-point method is obtained from the Newton-Raphson method by avoiding the first derivative terms inside $\frac{dr_{h,n}(h^{n+1,m}, v)}{dh^{n+1,m}}$. The damped Newton-Raphson method relaxes the increment $\delta_h^{n+1,m}$ while the new residual is greater than the previous one. Such a procedure is described in [12]. One important choice for nonlinear iterative process is the stopping criterion which is set for this study as:

$$\frac{\|r_{h,n}(h^{n+1,m}, v)\|_{L^2(\Omega)}}{\|a_{h,n}(h^{n+1}, v)\|_{L^2(\Omega)}} < \varepsilon_1 \quad \text{and} \quad \frac{\|\delta_h^{n+1,m}\|_{L^2(\Omega)}}{\|h^{n+1,m}\|_{L^2(\Omega)}} < \varepsilon_2, \quad (29)$$

where $\varepsilon_1, \varepsilon_2$ are a user-defined tolerances.

3.4 Adaptive time stepping

Time adaptation is motivated by the convergence of the nonlinear solver. On one hand, transient simulations have difficulties to converge if the time step is too large but, on the other hand, shorter time steps mean more time steps and so, a longer computational time. That is the reason why time adaptation is very attractive and common for Richards' equation. Different strategies can be used to adjust the time step [18], either heuristic and mainly based on convergence performance of the nonlinear solver or rational and based on error control. The latter ones are generally more efficient but heuristic methods remains a relevant approach owing to their simplicity.

For this study, the time step is adjusted heuristically according to the previous number of iterations N_{it} from the nonlinear solver such as [3, 47]. The simulations begins with a time step τ^0 . The next time step τ^{n+1} is calculated from the previous one τ^n according to the time-stepping scheme:

$$\begin{cases} \tau^{n+1} = \begin{cases} \lambda_{amp} \tau^n & \text{if } N_{it} \leq m_{it}, \\ \tau^n & \text{if } m_{it} < N_{it} \leq M_{it}, \\ \lambda_{red} \tau^n & \text{if } M_{it} < N_{it} \leq W_{it}, \end{cases} \\ \tau^n = \lambda_{red} \tau^n \text{ if } W_{it} < N_{it} \text{ or if the solver has failed (time step is started again).} \end{cases} \quad (30)$$

The factors $0 < \lambda_{\text{red}} < 1$ and $1 < \lambda_{\text{amp}}$ as well as the threshold values $0 < m_{\text{it}} \leq M_{\text{it}} < W_{\text{it}}$ are prescribed by the user. A minimum time step is defined to avoid excessive small time step.

With this approach, the nonlinear solver is more robust because the time step is adjusted until success of convergence whatever τ^0 . Thanks to the amplification/reduction coefficients, the time step is adjusted smoothly. Nevertheless, the method depends on fixed empirical parameters and does not provide an optimal time step. The resulting loss/gain in computational time is difficult to assess in regards to balance between nonlinear iterations number and time steps length.

4 Adaptive strategy

4.1 Adaptive Mesh Refinement

The Adaptive Mesh Refinement techniques (AMR) are now widely used and have since proven their efficiency, whether on 2D or 3D mesh, structured or unstructured mesh, conforming or not conforming mesh, with domain decomposition or not, see *e.g.* [33, 29, 20, 9].

In this work, applications with complex geometries are aimed, or even later couplings of models on hybrid mesh. This is why, as in a previous work [1], a non conforming unstructured mesh is used. Therefore, although computing time may be lost compared to fully structured Cartesian codes, Block-Based Adaptive Mesh Refinement strategy is adopted. In accordance with the simulations presented in this paper, only the bidimensional case is presented. The strategy adopted is then as follows and illustrated in the Fig. 2.

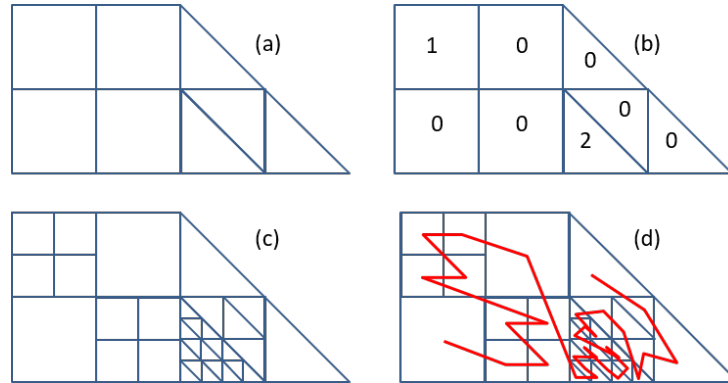


Figure 2: AMR Strategy: (a) Block mesh; (b) Level of mesh refinement; (c) mesh generation; (d) Morton numbering.

The unstructured mesh is composed of quadrilateral and/or triangular elements, where each element, as in [1], defines a *root element* or *block*, see Fig. 2(a). Then, a mesh refinement level is defined for each block, initially by the user and thereafter in accordance with the chosen mesh refinement criterion, see Fig. 2(b). Coarsening and refinement are decided according to threshold values $0 < \beta_c < \beta_r$. The mesh refinement level is adapted according to the rule that the ratio of mesh refinement should not exceed 2 between two neighbouring blocks. As illustrated in [17], this constrain allows smooth transitions between refined and unrefined regions. The mesh is then build using a quadtree graph (available for quadrangle and triangle) in order to define easily and precisely the neighbouring elements of each face. This procedure is pursued until the desired level of mesh refinement is reached as shown in Fig. 2(c). In the case of evolutionary problems, this implies frequent remeshing to follow the phenomenon studied. This is why, we prefer to widen the stencil with a coarse root mesh, namely blocks, and therefore to use

the whole quadtree graph, in order to remesh less often. It is illustrated for quadrangles and triangles in Fig. 3. Finally, a space filing curve using Morton numbering (Z-order) is build in order to number easily the degrees of freedom line in Fig. 2(d).

During a simulation, if a mesh refinement or coarsening process takes place, a new evaluation of the unknown field must be carried out. The prolongation (refinement) and restriction (coarsening) process are facilitated by the fact that the quadtree graph connect explicitly the "mother" element to its four "daughter" elements. To do that, one may use local interpolation/extrapolation. This is not straightforward in practice because it requires to identify the number of points and their position on the element to construct a right-determined system giving a fairly close solution. In the present study, the projection is made by solving a local DG problem. This technique gives good degrees of freedom by performing calculations at quadrature points. The element-wise weak formulation corresponding to $h_{E_{\text{new}}} = h_{E_{\text{old}}}$ reads:

$$\int_{E_{\text{new}}} h_{E_{\text{new}}} v \, dE_{\text{new}} = \int_{E_{\text{old}}} h_{E_{\text{old}}} v \, dE_{\text{old}}. \quad (31)$$

180 Then, mass matrix can be used to project the solution on the new mesh. This method is also used to enforce the initial condition $h = h_0$.

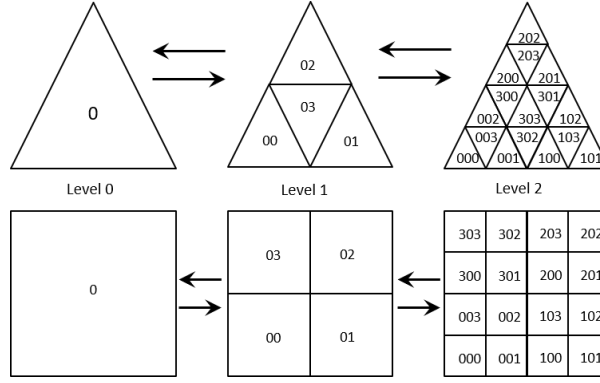


Figure 3: Mesh refinement for quadrangle and triangle using quadtree.

4.2 *A posteriori* error estimation

An *a posteriori* error indicator is employed to show how a simple quantity linked to problem physics is able to provide information about refinement. This error indicator is inspired from Miller *et al.* [32] where they use changes in effective saturation. Here, the error indicator is based directly on changes in the solution that is to say the gradient of hydraulic head h . This allows to work both for the saturated and unsaturated regions. So, it writes:

$$C_E = \frac{1}{\max_{E \in \mathcal{E}_h} \left(\frac{1}{|E|} \|\nabla h\|_{L^2(E)} \right)} \frac{1}{|E|} \|\nabla h\|_{L^2(E)}. \quad (32)$$

The error indicator is normalized so that $0 \leq C_E \leq 1$.

185 Another *a posteriori* error indicator is introduced but it is based on error estimation. Indeed, Verfürth developed *a posteriori* estimation-based error indicators based on residual and derived thanks to suitable norms in the context of finite elements methods for many equations [56], in particular for nonlinear parabolic problems such as Richards' equation. For this kind of problem, Verfürth used some variants to prove reliability as well as global and local efficiency for implicit Runge-Kutta schemes with some restrictions [55] and more standard time discretization in

190 [53, 54]. Later on, this type of residual-based derivation was adapted by Melenk and Wohlmuth to hp -adaptive finite elements methods for elliptic problems [31]. Afterwards, Houston *et al.* [22] as well as Schötzau and Zhu [40, 58] developed residual-based *a posteriori* error estimation for hp -adaptive interior penalty DG methods applied to elliptic problems and convection-diffusion equations respectively.

Greatly inspired by these works and supported by an heuristic analysis, the following *a posteriori* estimation-based error indicator is used:

$$\eta_E^{n^2} = \eta_{R_E}^{n^2} + \eta_{F_E}^{n^2} + \eta_{J_E}^{n^2}, \quad (33)$$

where the element residual, the face residual and the solution jump are respectively:

$$\eta_{R_E}^{n^2} = \frac{h_E^2}{p_E^2 \lambda_m(\mathbb{K})} \left\| \frac{\theta(u_h^{n+1}) - \theta(u_h^n)}{\tau^n} - \nabla \cdot (\mathbb{K}(u_h^{n+1}) \nabla u_h^{n+1}) \right\|_{L^2(E)}^2, \quad (34)$$

$$\begin{aligned} \eta_{F_E}^{n^2} = & \sum_{F \in \partial E \cap \mathcal{F}_h^I} \frac{h_F}{2p_F \kappa_m} \left\| \llbracket \mathbb{K}(u_h^{n+1}) \nabla u_h^{n+1} \cdot \mathbf{n} \rrbracket \right\|_{L^2(F)}^2 \\ & + \sum_{F \in \partial E \cap \mathcal{F}_h^N} \frac{h_F}{p_F \min(\kappa_l, \kappa_r)} \left\| q_N - \mathbb{K}(u_h^{n+1}) \nabla u_h^{n+1} \cdot \mathbf{n} \right\|_{L^2(F)}^2, \end{aligned} \quad (35)$$

$$\begin{aligned} \eta_{J_E}^{n^2} = & \sum_{F \in \partial E \cap \mathcal{F}_h^I} \left(\frac{\varrho_F^I}{2} + \frac{h_F}{p_F \kappa_m} \right) \left\| \llbracket u_h^{n+1} \rrbracket \right\|_{L^2(F)}^2 \\ & + \sum_{F \in \partial E \cap \mathcal{F}_h^D} \left(\varrho_F^D + \frac{h_F}{p_F \kappa_m} \right) \left\| u_D - u_h^{n+1} \right\|_{L^2(F)}^2. \end{aligned} \quad (36)$$

The quantities $\lambda_m(\mathbb{K})$ and $\lambda_M(\mathbb{K})$ stand respectively for the lowest and largest eigenvalue of \mathbb{K} on E . For a face F of normal \mathbf{n} , the minimum of normal component from neighbouring \mathbb{K} is chosen: $\kappa_m := \min(\kappa_l, \kappa_r)$ where $\kappa = \mathbf{n}^\top \cdot \mathbb{K}(u_h^{n+1}) \cdot \mathbf{n}$. Here, the time discretization is based on the implicit Euler scheme but the *a posteriori* estimation-based error indicator can be determined for other time schemes such as in [55]. Global estimates are obtained with:

$$\eta^{n^2} = \sum_{E \in \mathcal{E}_h^n} \eta_E^{n^2}. \quad (37)$$

195 Unlike the aforementioned papers, there is no rigorous mathematical proof for this residual-based energy norm *a posteriori* error estimation. Extension to the case of nonlinear and time-dependant parabolic equation solved by hp -adaptive DG methods remains an open problem. However, some remarks can be drawn. Firstly, the numerical treatment of the time dependence and of the nonlinearity resorts to consider a sequence of linear and steady problems. Secondly,
200 as noted by Verfürth [56], the element residual term is related to the residual of the numerical solution with respect to the strong form of the equation which may be viewed as the error from the nonlinear process. The face residual term is related to the boundary operator which is associated with the strong and weak forms of the differential equation. It reflects, on one hand, that the numerical solution gradient – the flux – is discontinuous and on the other hand,
205 that Neumann boundary conditions may not be satisfied. The solution jump term is related to the penalization which are associated with the weak form of the equation. It reflects that the numerical solution is discontinuous at interior faces in the DG framework and Dirichlet boundary conditions may be slightly violated according to the penalty coefficients. Moreover, the second term and third parts of the estimation-based error indicators measure how valid the
210 hypothesis on the seek solution are to derive the DG formulation.

4.3 Weighted discontinuous Galerkin framework

In the context of convection-diffusion equations or coupling of parabolic/hyperbolic domains, the solution may hold spurious oscillations at internal layers for vanishing or varying diffusion [16]. This situation is typical of porous media problems where there are material heterogeneity and degenerate hydraulic properties. One interpretation is the flow stays continuous but the solution mimics a discontinuity. Then, the numerical scheme is unable to recognize the sharp internal layer leading to numerical instabilities.

Even though this phenomenon may be resolved by mesh refinement, the corresponding computational cost is substantial to maintain a physically acceptable solution. Slope limiters are another possibility to control these undershoots/overshoots but further computational developments are needed to cope with the geometry of elements in high-dimension [44, 39]. A satisfactory approach would be to design a DG method that can handle internal layers in an automated fashion. That is the reason why the weighted discontinuous Galerkin (WDG) framework was introduced [15, 39]. These methods work thanks to two key ingredients which can be seen as a way to incorporate into the definition of the scheme some partial knowledge of the solution. The first one is the use of weighted averages instead of the standard arithmetic average inside the discontinuous formulation. Then, the amount of diffusivity flux for each side of a face is controlled. The second ingredient is to relax the face penalization used for continuity constraint by a coefficient depending on the harmonic mean of the diffusivity of the neighbouring elements. Such a penalty strategy turns out to tune automatically the amount of local penalty to regulate the degree of smoothness of the approximate solution. Analysis and details can be found in [15, 39] and related.

Internal layers depend on the spectral structure of the diffusivity. The choice is to take its normal component for face evaluation [15, 6]. Weights across a face are positive numbers such that $\omega_l + \omega_r := 1$. The weighted average and the conjugate weighted average are respectively defined as:

$$\llbracket u \rrbracket_\omega := \omega_l u_l + \omega_r u_r, \quad \llbracket u \rrbracket_{\bar{\omega}} := \omega_r u_l + \omega_l u_r. \quad (38)$$

Then, the relation $\forall u, v \in S_p(\mathcal{E}_h^n)$, $\llbracket uv \rrbracket = \llbracket u \rrbracket_\omega \llbracket v \rrbracket + \llbracket u \rrbracket \llbracket v \rrbracket_{\bar{\omega}}$ is replacing Section 3.1 in the weak formulation derivation. The weighted diffusion penalty coefficient is taken to be the weighted average of diffusivities which results to be equivalent to the harmonic mean of the neighbouring normal hydraulic conductivities across the face [15]:

$$\gamma_F = \llbracket \kappa \rrbracket_\omega = \frac{2\kappa_l \kappa_r}{\kappa_l + \kappa_r}. \quad (39)$$

Standard DG methods assume $\omega_l = \omega_r = \frac{1}{2}$, which reduces the weighted average to the arithmetic average, and $\gamma_F = 1$. The WDG method chooses other definitions. Following definitions in [15], let the weights be:

$$\begin{cases} \omega_l = \frac{\kappa_r}{\kappa_l + \kappa_r}, & \omega_r = \frac{\kappa_l}{\kappa_l + \kappa_r} & \text{if } \kappa_l + \kappa_r \neq 0, \\ \omega_l = \omega_r = \frac{1}{2} & & \text{otherwise.} \end{cases} \quad (40)$$

WDG methods assume that diffusivity discontinuities fit the mesh [15]. This is generally the case for heterogeneous media but it is not true for nonlinear diffusivity such as in Richards' equation. Then, sharp internal layers may occur inside an element so the weighted framework is not expected to work in this situation. Nevertheless, a suitable adaptive mesh refinement can be used as a capturing technique. This idea is one of the main novelties proposed in this paper. The weighted framework and mesh adaptation are working dynamically in synergy: the former

changes the smoothness nature of the numerical solution while the latter tracks the internal layer linked to nonlinearity thanks to refinement driven by the *a posteriori* estimation-based error indicator Eq. (33).

5 Numerical results

Simulations are performed to highlight some numerical behaviour of Richards' equation and the ability of the numerical methods to treat them. The IIPG method is employed in every simulation thereafter.

5.1 Polmann's test-case

This test-case considers a soil from New Mexico whose hydraulic properties are provided by Polmann *et al.* [36]. A 1D vertical sample of this soil subject to downward infiltration was simulated by Celia *et al.* [7], Manzini and Ferraris [30] as well as Sochala [44]. This test-case can be challenging because, on one hand, the prescribed pressure head on both sides of the 100 cm soil column has a difference of 925 cm resulting in steep solicitation, and, on the other hand, hydraulic conductivity shows strong variations under the set of values taken by pressure head. The Polmann's test-case employs Van Genuchten-Mualem relations with $K_s = 9.22 \times 10^{-3} \text{ cm} \cdot \text{s}^{-1}$, $\theta_s = 0.368$, $\theta_r = 0.102$, $\alpha = 3,35 \times 10^{-2} \text{ cm}^{-1}$, $n = 2$, $m = 0.5$ and $l = 0.5$. The computational domain Ω is a rectangle $(0, 20) \times (0, 100) \text{ cm}$. The test-case is solved for pressure head ψ during $T = 172800 \text{ s}$ (48 h) with a constant time step $\tau = 120 \text{ s}$ and the initial condition is $\psi_0 = -1000 \text{ cm}$. Throughout the examples, implicit Euler scheme, $p = 1$, $\sigma_I = \sigma_B = 100$ are used. Computation is done for two meshes: M100 is a coarse mesh of 100 elements and M1000 is a refined mesh of 1000 elements.

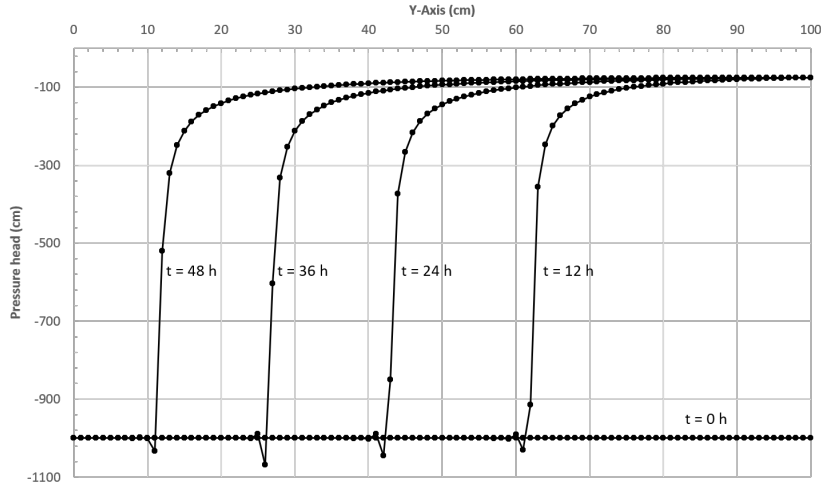


Figure 4: Pressure head along the vertical for Polmann's test-case with the mesh M100.

For the mesh M100, nonlinear iterations have difficulties to reach the requirements of stopping criteria and the solution holds spurious oscillations, in particular an undershoot ahead of the sharp wetting front as showed in Fig. 4. This behaviour was already noticed by Celia *et al.* [7] and Sochala [44]. The latter decides to eliminate this undershoot by adding a slope limiter which causes a small late compared to the non-limited solution. Better results are obtained with the mesh M1000, the oscillations in the solution vanish, see Fig. 5. The M1000-results agree with those from Celia *et al.* [7] as well as from Manzini and Ferraris [30]. This shows

that a good discretization is necessary for Richards' equation to get quality solution. Such requirement can be fulfilled at optimal cost by a suitable adaptive local refinement. The error indicator from Eq. (32) is employed with refinement threshold values $\beta_c = \beta_r = 50$. Adaptation is performed every 5 time steps, starting with the M100 mesh. In Fig. 5, results show that refinement is able to capture the wetting front dynamically and eliminate the undershoot. The average number of elements is 211. More frequent adaptations allow to follow perfectly the front while less frequent adaptations are less costly.

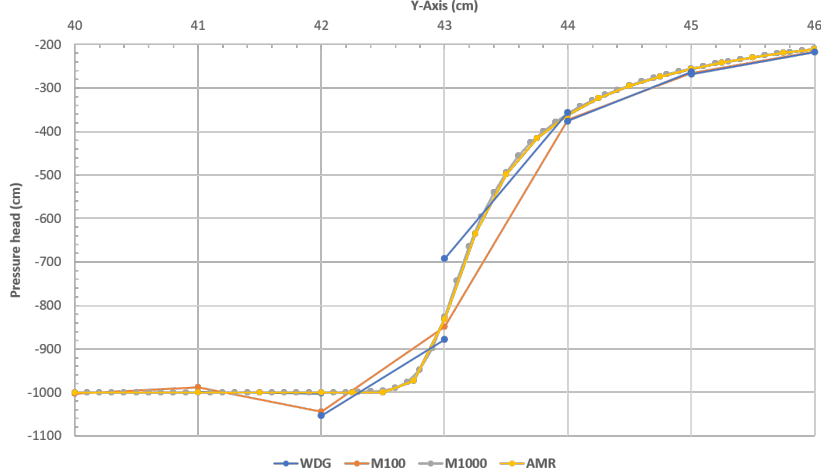


Figure 5: Comparison of pressure head at $t = 24$ h for Polmann's test-case: IIPG on mesh with 100 elements (M100), IIPG on mesh with 1000 elements (M1000), IIPG with adaptive mesh refinement (AMR), WDG with 100 elements (WDG).

In addition, the WDG method from section 4.3 is tried without any adaptation. The mesh M100 is used. Results in Fig. 5 show that the undershoot is still present but reduced to one single element. It is relevant to point out that the solution holds jumps where the wetting front is steep. They prevent oscillations to propagate and make solution catch the front steepness. The remaining undershoot depends on the wetting front localization in relation with the mesh geometry. This is due to the nonlinear nature of diffusivity and that is why it is important to associate mesh adaptation.

5.2 Tracy's benchmark

This test-case has an analytical solution given by Tracy [48] for 2D and 3D problems which can be used as a benchmark for Richards' equation [49, 50]. Tracy's benchmark is particularly relevant because it is transient, has a simple parameter to vary nonlinearities for Richards' equation and holds differentiated steep regions. It can serve to check the nonlinear solver robustness, convergence properties and adaptive mesh refinement. Then, it is very convenient to assess the solution quality and compare codes: Šolín and Kuraz [45] and Dolejší *et al.* [12] used it to evaluate the performance of their respective method.

Tracy's benchmark employs Gardner-Irmay relations with $K_s = 1.1 \text{ m}\cdot\text{d}^{-1}$, $\theta_s = 0.5$, $\theta_r = 0$, $\alpha = 0.1 \text{ m}^{-1}$ and $m = 1$. It is solved for pressure head ψ . The residual pressure head ψ_r is a parameter. The computational domain Ω is a square $(0, a) \times (0, b)$ m. Here, $a = b = 1$ m and $\psi_r = -10$ m. A specific Dirichlet boundary condition is prescribed on the top edge with the function:

$$\psi_{\text{top}} = \frac{1}{\alpha} \log \left(e^{\alpha \psi_r} + \left(1 - e^{\alpha \psi_r} \right) \sin \left(\frac{\pi x}{a} \right) \right). \quad (41)$$

While for other edges, a constant Dirichlet boundary condition is imposed: $\psi = \psi_r$. The initial condition is $\psi_0 = \psi_r$. Tracy gives the 2D exact solution ψ_{ex} in [48]. Figure 6 shows the solution obtained for a fixed grid with $\tau = 10^{-4}$ day and $T = 10^{-2}$ day.

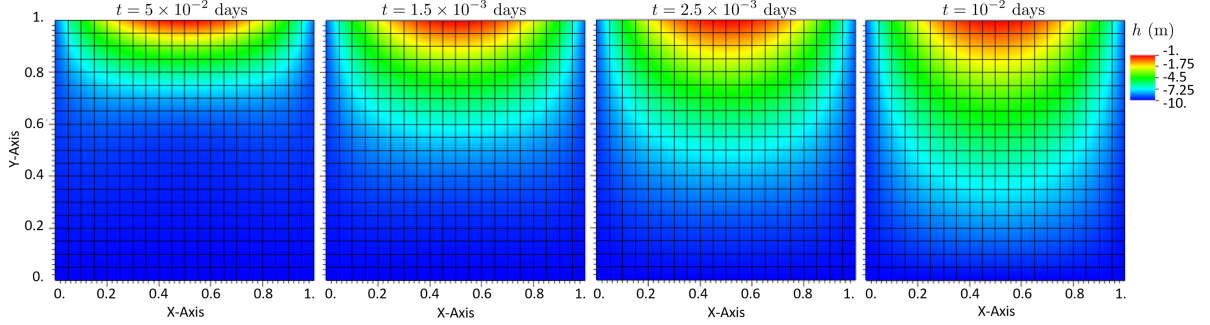


Figure 6: Hydraulic head for Tracy's benchmark with $p = 1$ and 6-step BDF.

The treatment of initial condition is not straightforward. First, because the initial condition does not respect the top boundary condition: they are inconsistent. This issue can be troublesome for discretizations like finite elements methods [45] but it is natural for DG methods where boundary conditions are usually enforced by weak penalization [12]. Second, because the top boundary condition condition is particularly stiff compared to the initial state. Therefore, the very first moments are the most interesting to simulate in order to address the time-boundary inconsistency and the early stiffness. Nonlinearities are controlled by the parameter α in Eq. (41). More α is large, more the relative hydraulic conductivity drops quickly to near zero, and so, nonlinearities are increased for Richards' equation [49]. Moreover, errors are linked to the top corners since the top boundary condition induces a steep slope at these corners [49, 50]. As Tracy stated, these features make this problem a good option to investigate adaptive mesh refinement.

The classic L^2 -norm and the energy norm, also called the DG intrinsic norm, are introduced:

$$\|u\|_{L^2(E)}^2 := \int_E u^2 \, dE \quad \|u\|_{\mathcal{E}(E)}^2 := \|u\|_{R(E)}^2 + \sum_{F \in \partial E} \|u\|_{J(F)}^2, \quad (42)$$

where the residual seminorm and the jump seminorm are respectively:

$$\|u\|_{R(E)}^2 := \int_E \mathbb{K}(u) \nabla u \cdot \nabla u \, dF = \left\| (\mathbb{K}(u))^{\frac{1}{2}} \nabla u \right\|_{L^2(E)}^2, \quad (43)$$

$$\|u\|_{J(F)}^2 := \int_F \varrho_F [u]^2 \, dF = \varrho_F \| [u] \|_{L^2(F)}^2. \quad (44)$$

Errors between numerical and exact solution are computed for a time step such that:

$$\|e\|_X = \|\psi_{\text{ex}} - \psi\|_X \quad \text{with } X = \{L^2, \mathcal{E}, R, J\}. \quad (45)$$

To measure how effective the estimation-based error indicator is, the effectivity indices for the estimation-based error indicator (33), the element and face residuals (34, 35), and the solution jump (36) will be used:

$$I_{\mathcal{E}}^{\text{eff}} := \frac{\eta_E^n}{\|e\|_{\mathcal{E}(E)}}, \quad I_R^{\text{eff}} := \frac{(\eta_{R,E}^{n,2} + \eta_{F,E}^{n,2})^{\frac{1}{2}}}{\|e\|_{R(E)}}, \quad I_J^{\text{eff}} := \frac{\eta_{J,E}^n}{\|e\|_{J(F)}}. \quad (46)$$

Due to the lack of rigorous derivation, the effectivity index is not expected to represent properly the true error. The estimator efficiency is rather appreciated to set up a mesh refinement strategy.

First of all, several simulations are performed to show convergence properties. Because of symmetry, one half vertical plan of the domain is considered to speed up the simulation. Duration is set to $T = 10^{-4}$ day to focus on small times. The computations are carried out with the 6-step BDF and time steps are set to $\tau = 10^{-6}$ s. This is needed to reduce time discretization errors expecting that they will be negligible compared to space discretization errors in order to observe space convergence. Indeed, according to theoretical error estimates [11], error in L^2 -norm and H^1 -seminorm behave such that:

$$\|e\|_{L^2} \approx c_h h^p + c_\tau \tau^q, \quad (47)$$

$$\|e\|_{\mathcal{E}} \approx c'_h h^{p+1} + c'_\tau \tau^q, \quad (48)$$

where c_h , c'_h , c_τ and c'_τ are constants independent of h and τ . Numerical experiments involve four meshes of 50, 200, 400 and 3200 quadrilateral elements. Order approximation varies from one to four. Figure 7 shows the convergence of the error e_h for the L^2 - and energy norms with respect to the number of degrees of freedom. It is interesting to note that space error are so small for the most dense mesh with $p = 4$ that time error saturates the convergence.

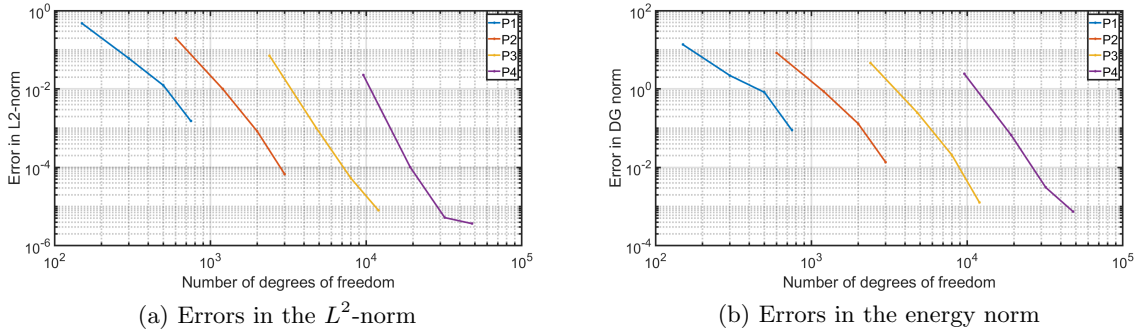


Figure 7: Numerical convergence for Tracy's benchmark.

In Fig. 8, effectivity indices are plotted. While the jump indicator (36) is very effective, the other estimation-based error indicator components are not representative of the true error in term of magnitude. Nevertheless, they always overestimate the true error which is good for mesh refinement monitoring. Behaviour of the three contributions with respect to the number degrees of freedom by varying the order of approximation and the mesh size is shown in Fig. 8. Since they do not represent properly the true error, observations are difficult to put in touch with the true error. However, one can see that the volume contribution – the residual indicator – behaves quite differently compared to the surface contributions – the flux and jump indicators. The convergence is globally maximised with p -refinement for the surface contributions while h -refinement seems to improve convergence better for the volume contribution. This observation should be assessed more but could drive the hp -decision making.

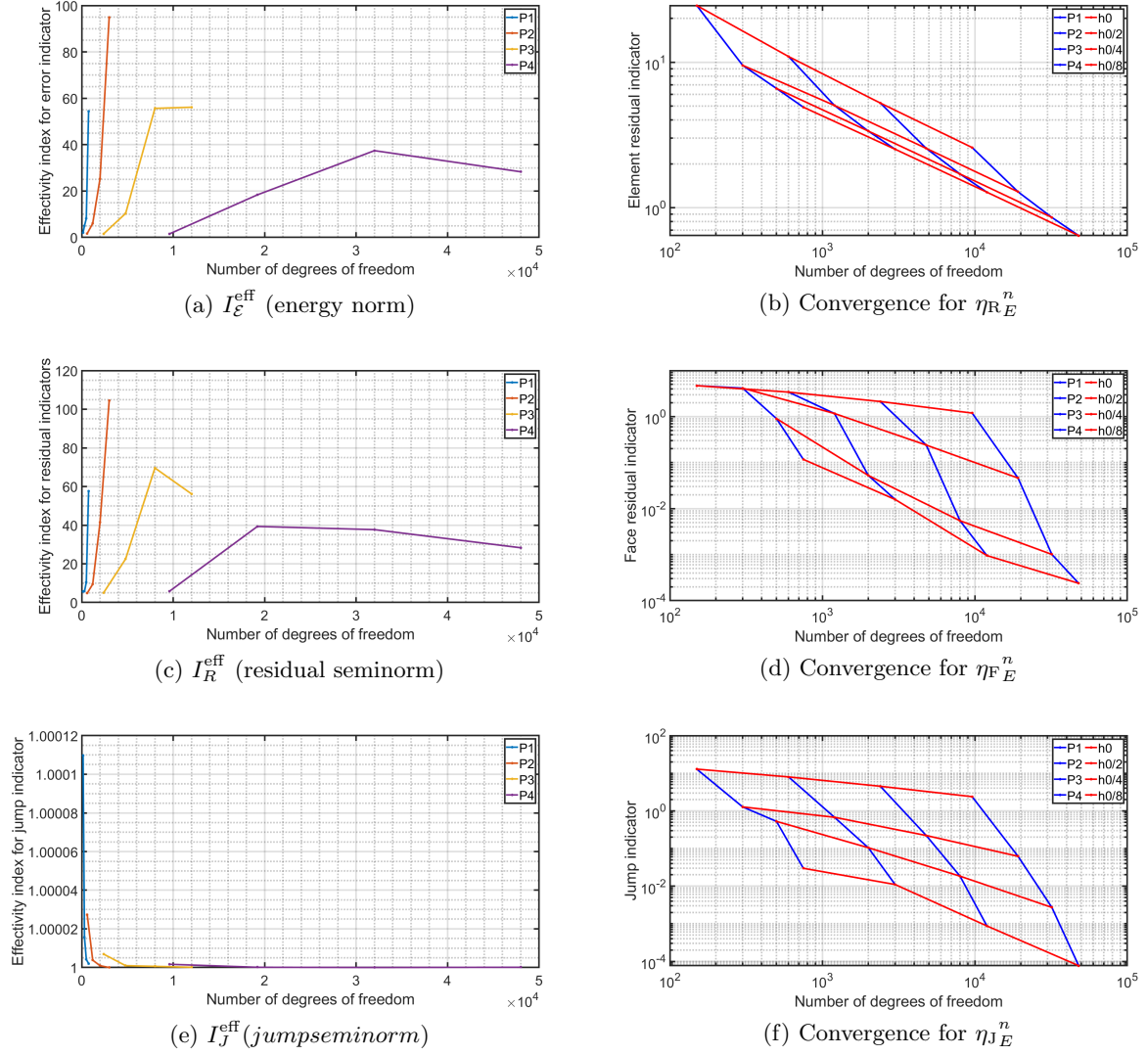


Figure 8: Effectivity indices for different indicators (left) and convergence diagrams for the three parts of the indicator η_E^n (right).

Error estimation is evaluated in terms of ability to drive the mesh adaptation. The error in L^2 -norm is above the error measured with energy norm as stated in Fig. 9. It is worth to notice that the estimation-based error indicator is able to give the shape of the true error for the energy norm, particularly for steady state, see Fig. 10. Besides, the estimation-based error indicator spots the error in the top corner where Tracy stated there were problems for this test-case with $\beta_c = \beta_r = 0.5$. The gradient-based error indicator was used in a previous paper [8] to capture the moving wetting front on a simple 1D infiltration case. Yet, as shown in Fig. 11, it performs badly for the Tracy’s benchmark where steep gradients arise on a large part of the domain. The refinement thresholds are difficult to tune which leads to over-refinement for large regions at the top. They were set up to $\beta_c = \beta_r = 0.5$. Then, the computation is very costly. For the estimation-based error indicator, the ability to drive the mesh adaptation is more convincing. The mesh is adapted dynamically without inducing over-refinement. Elements are refined where it is needed because adaptation occurs locally while the error is controlled. Then, the cost is reasonable.

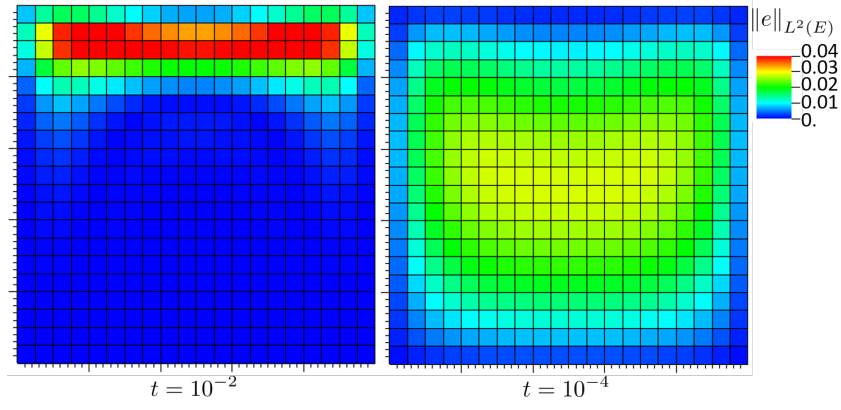


Figure 9: True error distribution in the L^2 -norm on Tracy's benchmark.

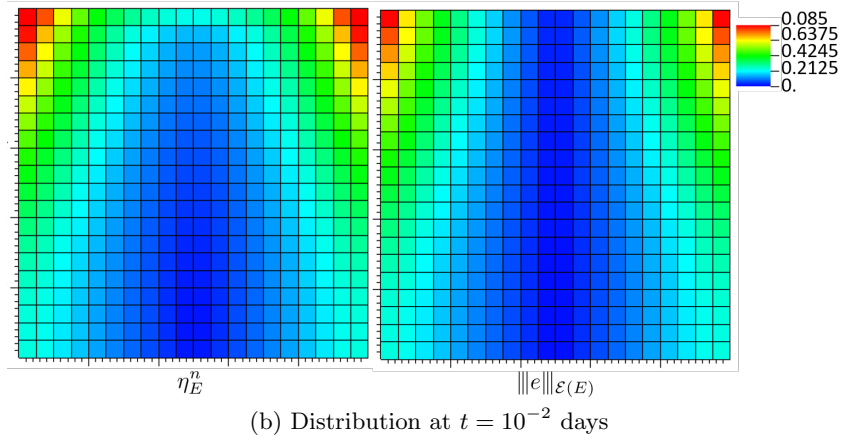
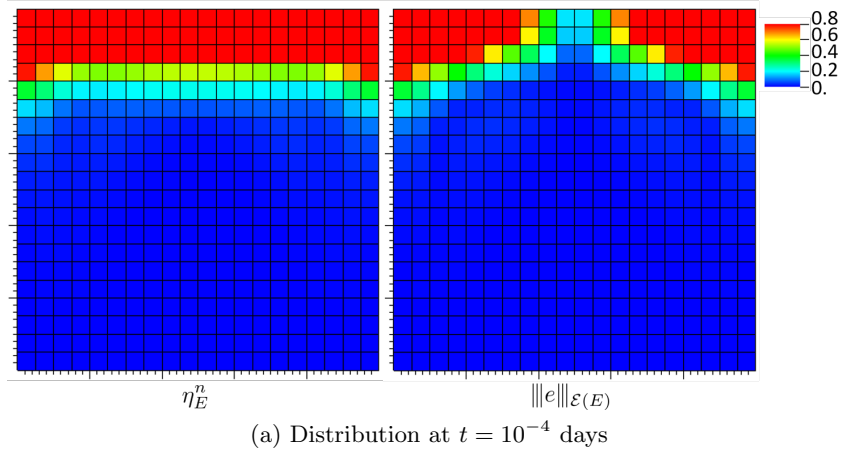
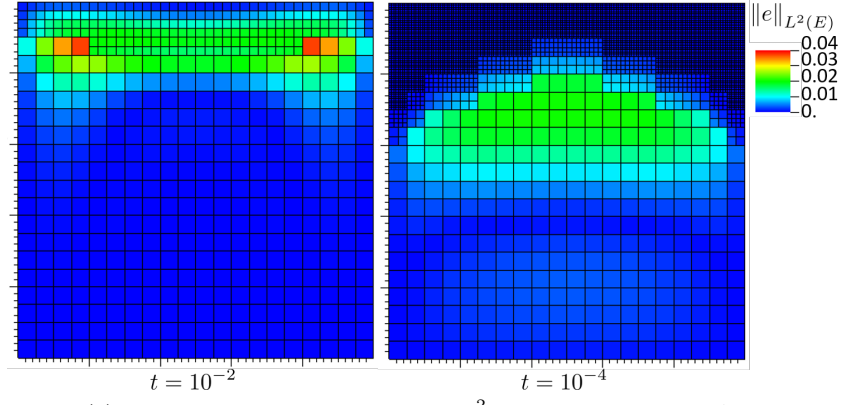
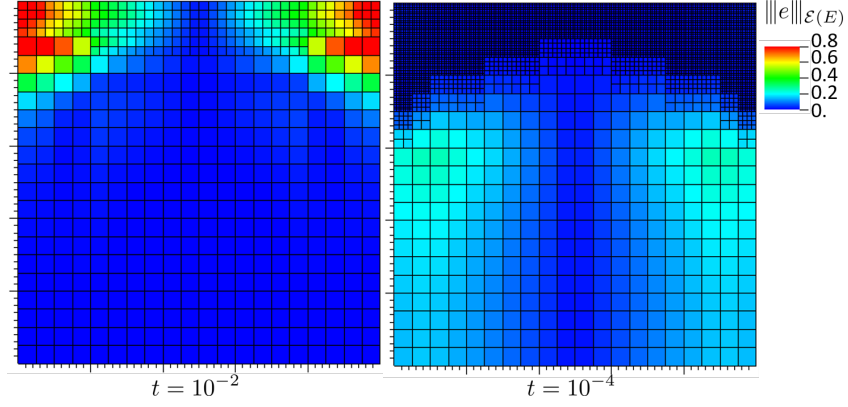


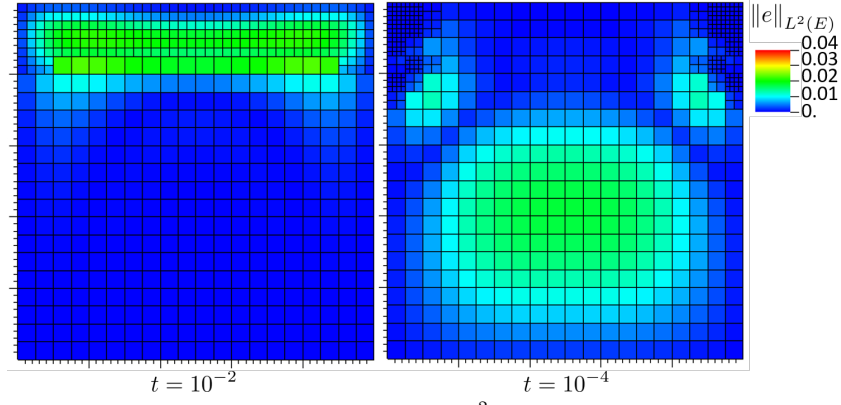
Figure 10: Comparison between distributions of true error in energy norm with the indicator η_E^n on Tracy's benchmark.



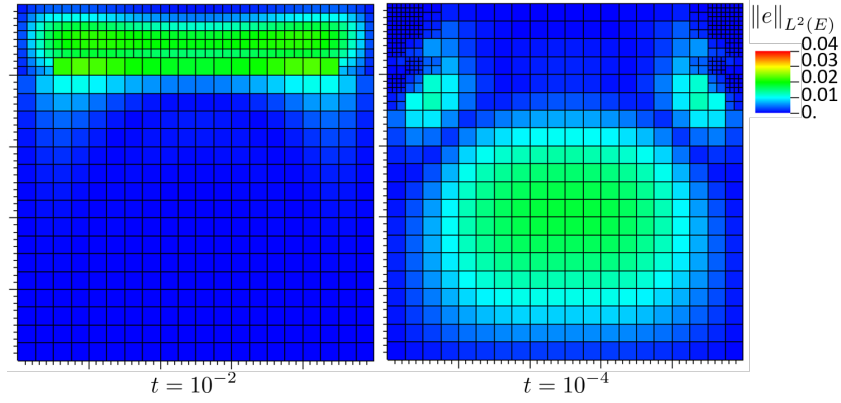
(a) Mesh and error distribution in L^2 -norm for C_E -driven AMR



(b) Mesh and error distribution in energy norm for C_E -driven AMR



(c) Mesh and error distribution in L^2 -norm for η_E^n -driven AMR



(d) Mesh and error distribution in energy norm for η_E^n -driven AMR

5.3 Wetting of the La Verne dam

5.3.1 Setting

The model is here used to simulate the full-scale wetting of a multi-materials dam: the La Verne dam. La Verne dam was constructed in 1991 to supply Gulf of Saint-Tropez (south of France) with drinkable water. La Verne dam is 42 m high and peaks at 90 m above sea level. Its width ranges from -102.3 m to 110.5 m. The reservoir is on the left in Fig. 12. The genuine La Verne dam inner section shows a complicated heterogeneous material patterns, partially described in [19, 4]. The dam is an earth-filled embankment dam. A clay core allows for impermeability while outer zones are semi-permeable alluvial shells. The dam is protected by rip-rap upstream. Filters and drains of very permeable gravel-like materials secure the dam inner saturation. The dam foundation lies on an impervious rock stratum thanks to concrete injections. A fine loam layer covers the downstream dam part. The filling of La Verne dam was controlled with instruments [19] during 40 days, which provides a unique and challenging dataset to test the model. In particular, the reservoir height evolution is available as well as three groundwater hydraulic head measurements from the core, see Fig. 12 and 14. The three gauges are at $z = 55$ m and their x-coordinates are -10.5 m, -3 m and 5 m.

For the simulation, the reservoir height is used as a forced boundary condition in the form of a Dirichlet boundary condition monitored by a function based on experimental data (see Figure 13). Since comparison focusses on the core of the dam, it is assumed that outer high permeable and/or fine layers materials do not have a significant impact on inner groundwater flows and saturation. The downstream thin loam layer, the filter-isolated toe drain and the lower submerged rip-rap are therefore not represented by the simulation and assimilated to the adjacent materials (see Tab. 4 for description of numerical dam structure). A Dirichlet boundary condition for hydraulic head is prescribed at the downstream boundary. The upper rip-rap and the cofferdam are simulated as such to assess the method robustness owing to their direct contact with the upstream dynamic boundary condition (forcing) and their hydraulic properties are steep. Rock/concrete foundations are supposed to be perfectly impervious which means a zero-valued Neumann boundary condition can be prescribed. Finally, seepage boundary condition are prescribed everywhere else because outflow can drain from the exposed upstream and downstream shell slopes. The actual simulated configuration of La Verne dam is sketched in Fig. 12. Five different materials are simulated (Tab. 4), with hydraulic properties provided by Bonelli *et al.* [4]. The dam wetting simulation involves each tool presented in this paper for the adaptive strategy: the WDG method in combination with the AMR technique driven by the estimation-based error indicator. Mesh adaptation is done every five time steps. Fixed-point iteration is used together with adaptive time stepping. Order of approximation is quadratic for space and one for time in order to have a robust and cost-effective computation. Penalty parameters are $\sigma_I = \sigma_B = 100$.

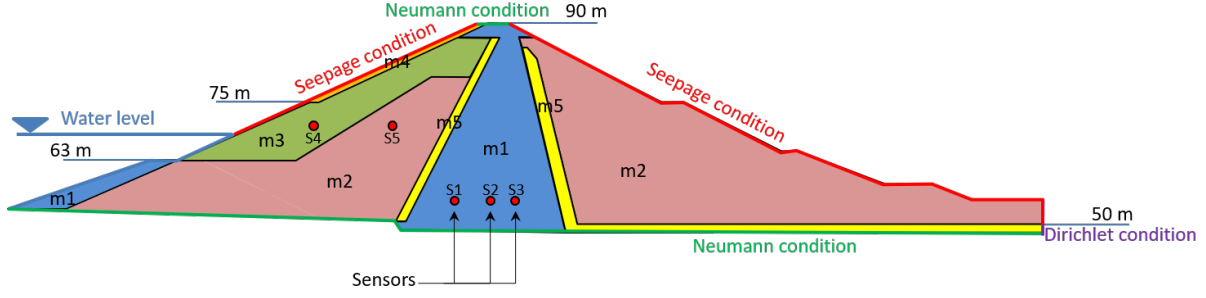


Figure 12: Geometry, materials and boundary conditions of La Verne dam for the numerical case. S1, S2, S3 are numerical gauges corresponding to the experimental sensors while S4 and S5 are additional purely numerical gauges.

Materials	Components	Constitutive laws	θ_s	θ_r	$\mathbb{K}_s(1,1) (m \cdot d^{-1})$	$\mathbb{K}_s(2,2) (m \cdot d^{-1})$	Specific parameters
m1	Core Cofferdam	Van Genuchten-Mualem	0.23	0	2.592×10^{-3}	8.64×10^{-4}	$\alpha = 0.08m^{-1}, n = 1.2, l = 0.5$
m2	Upstream shell Downstream shell	Van Genuchten-Mualem	0.25	0	5.184	1.728	$\alpha = 0.01m^{-1}, n = 2.1, l = 0.5$
m3	Outer upstream shell	Vachaud	0.22	0	5.184	1.728	$A = 2.99 \times 10^{-4}m^5, B = 5$ $C = 6.34 \times 10^{-2}m^{2.9}, D = 2.9$
m4	Protection rip-rap	Vachaud	0.27	0	17.28	8.64	$A = 2.99 \times 10^{-4}m^5, B = 5$ $C = 6.34 \times 10^{-2}m^{2.9}, D = 2.9$
m5	Filters Drains	Vachaud	0.32	0	17.28	8.64	$A = 2.99 \times 10^{-4}m^5, B = 5$ $C = 6.34 \times 10^{-2}m^{2.9}, D = 2.9$

Table 4: Materials of the numerical La Verne dam.

The simulation of La Verne dam case is a very challenging benchmark for numerical models, combining heterogeneous materials, steep constitutive laws and dynamic boundary conditions. However, despite of its interest, the La Verne dam benchmark remains only partly documented by in-situ instruments, precluding a comprehensive quantitative confrontation between observations and model. In particular, the hydraulic properties, which have a drastic effect on flow dynamics, remain approximative due to the absence of direct in-situ characterization. In addition, note that no initial in-situ values for water table elevation and saturation are available inside the dam, which can also strongly affect the subsequent evolution. For the present simulation, the initial water table is imposed at 67 m to fit the initial values of experimental hydraulic head. Finally, Bonelli *et al.* pointed out that hydromechanical coupling should be considered to be fully consistent with the real case, see [19].

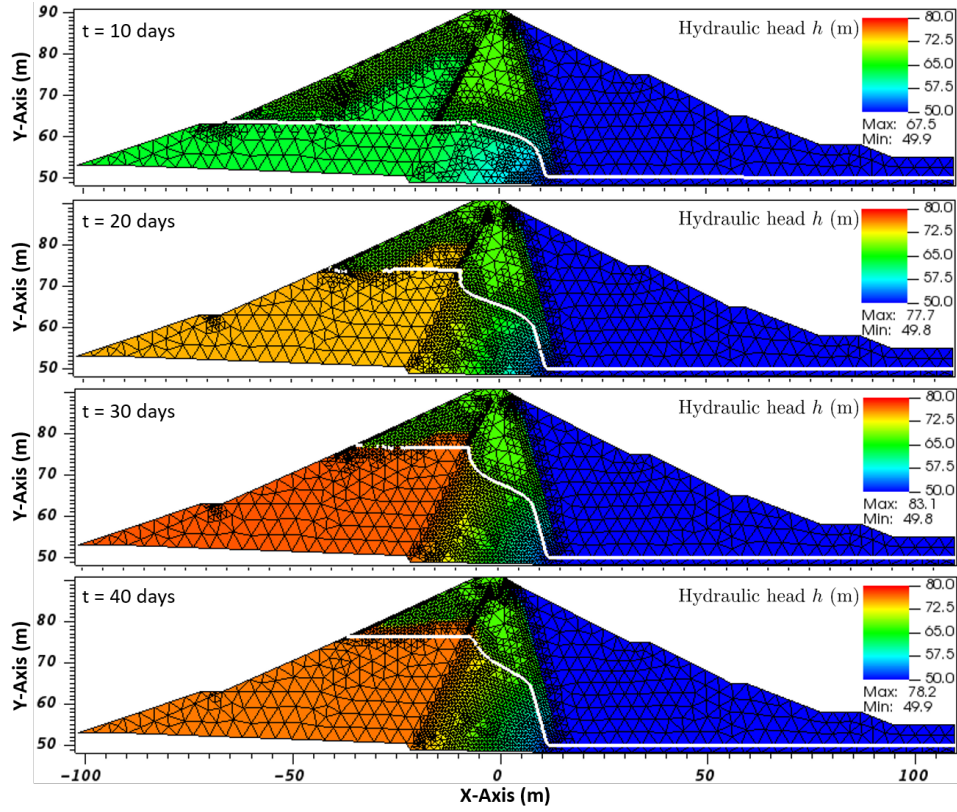


Figure 13: Time evolution of hydraulic head h , mesh and water table (white line) during La Verne dam wetting.

5.3.2 Results

Figure 13 depicts hydraulic head (color contours), water table (white line) and adaptive mesh for both simulations every 10 days. Time evolution of simulated hydraulic head and water content at the three experimental gauges (S1 to S3) and the two additional numerical gauges (S4 and S5) are displayed in Fig. 14. It is recalled that initial reservoir free surface and watertable elevation are at 57 and 67m, respectively. Note that the watertable is not displayed in Figure 13 at some points due to insufficient resolution and oscillations w.r.t the front sharpness, which are detailed in the Discussion section. The numerical model is observed to provide a good overall description of the dam wetting process. Figure 13 shows that the propagation of the wetting wave inside the dam is strongly dependent on the inner materials properties. The first eleven days are characterized by an adjustment phase during which the reservoir surface remains below the initial watertable elevation. Hydraulic head and water content at numerical gauges S4 and S5 show a very contrasting behavior (Fig. 14b and c). This reveals that, even if both m2 and m3 materials show the same hydraulic conductivity at saturation, the difference in constitutive laws induces a radically different dynamics of the capillary fringe. At S4, the head remains nearly constant during the adjustment phase while the water content is very low. The m3 material is here nearly desaturated, well above a thin capillary fringe. By contrast, S5 is within the large capillary fringe associated to the m2 material, providing a much higher water content. The hydraulic head shows first a small decay, probably due to the drain proximity, before starting to rise in response to the reservoir filling. Around day 14, both S4 and S5 gauges show a simultaneous regular rising, slightly lagged from the reservoir level. A strong jump is observed at S4 (Fig. 14c), indicating the crossing of a sharp capillary fringe. While rising, the

watertable remains nearly horizontal in the upstream m2-m3 materials zone but a sharp front is observed to develop across the left inner drain (m5 material), see Figure 13. Small numerical oscillations in hydraulic head are observed in Figure 14 but do not affect the global dynamics. Further downstream and lower within the dam, the hydraulic head simulated at S1, S2 and S3 shows the slow wetting wave propagation, with attenuation and damping (Figure 14b). At S1, S2, S3, the water content remains constant during the whole simulation, in accordance to the sensors position below watertable.

When compared to hydraulic head experimental data (see Fig. 14a), the overall time evolution and order of magnitude are well represented. Some discrepancies are observed, in particular the late increase of head which is experimentally observed on each gauge around 30 days, which tends to be underestimated by the model. However, recalling the lack of experimental control evoked before, more detailed comparison should be made with caution. For the sake of comparison, the previous numerical results presented by Bonelli *et al.* [4] are recalled in Figure 14 in green lines. While the overall time evolution is rather similar between models, a better agreement with experimental data is obtained with the present simulation.

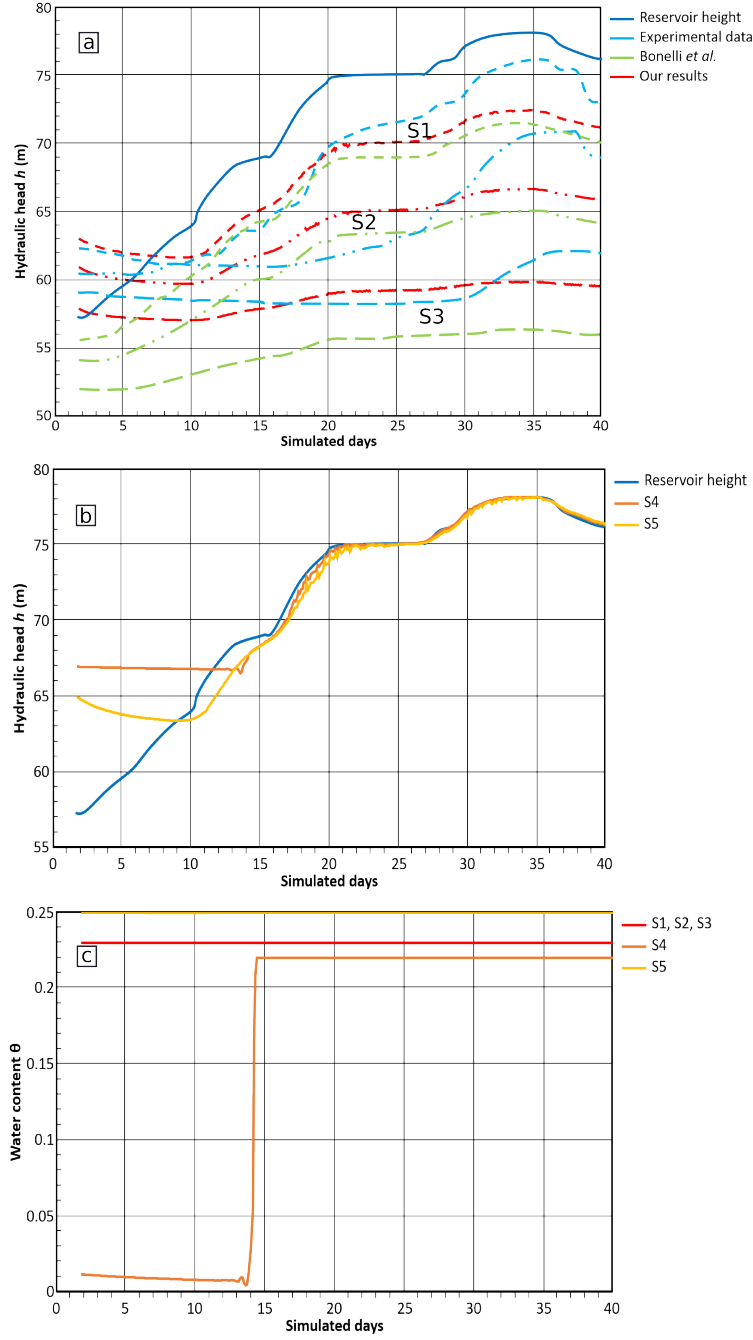


Figure 14: Time evolution of inner dam hydraulic parameters. a) Hydraulic head at gauges S1 (short-dashed lines), S2 (dash-dotted lines) and S3 (long-dashed lines) from the present simulation (red), the experimental data (light blue) and the previous results of Bonelli et al. [4]. The reservoir height is depicted in dark solid line. b) Hydraulic head at numerical gauges S4 (orange) and S5 (yellow). c) Water content at S1 to S5 gauges (note that S1, S2 and S3 show similar values).

5.4 Discussion

The proposed modeling strategy for Richard's equation showed very satisfactory performance in reproducing analytical and laboratory test cases and in simulating complex full-scale exper-

iment. In this latter case, the model is able to capture automatically wetting fronts which are moving dynamically thanks to AMR. In particular, the fronts associated with heterogeneity are well resolved by the WDG technique. This is illustrated by water content distribution in Fig. 15. Moreover, the simulation is robust since it is able to compute completely without user intervention and handle many features: degeneracy for saturated/unsaturated zones, dynamic forcing boundary condition and seepage. However, the simulation struggles to capture wetting fronts associated with nonlinear varying diffusivity resulting in severe overshoots/undershoots for the transition between saturated and unsaturated zones in very permeable materials. Further insight on this behaviour can be discussed using the Péclet number framework. Richards' equation is an elliptic-parabolic equation predominantly diffusive, it shares properties with convection-diffusion equation and can behave like them. For example, sharp wetting fronts and internal layers can be reinterpreted within this context. The Péclet number represents the ratio of the rate of advection to the rate of diffusion. This dimensionless number is useful to analyse locally the nature of the flow regime and determine whether advection or diffusion is dominant. For this study, the Péclet number is extracted from the saturation-based formulation of Richards' equation which is similar to a convection-diffusion equation with the water content θ as single unknown. This formulation is undefined in saturated zones because hydraulic diffusivity D tending to infinity but this zone is not of interest for the Péclet number since Richards' equation is purely diffusive. Moreover, it is assumed that $\theta \neq 0$. This assumption is not restrictive because if water content drops to zero, nothing happens and, in practice, there is often a residual water content. The total flux can be separated into a diffusive flux defined by hydraulic diffusivity and driven by capillarity, and an advective flux defined by hydraulic conductivity/water content and driven by gravity. The saturation-based formulation can be rewritten as:

$$\partial_t \theta - \nabla \cdot \left(D(\theta) \nabla \theta + \frac{\mathbb{K}(\theta) \nabla z}{\theta} \theta \right) = 0, \quad (49)$$

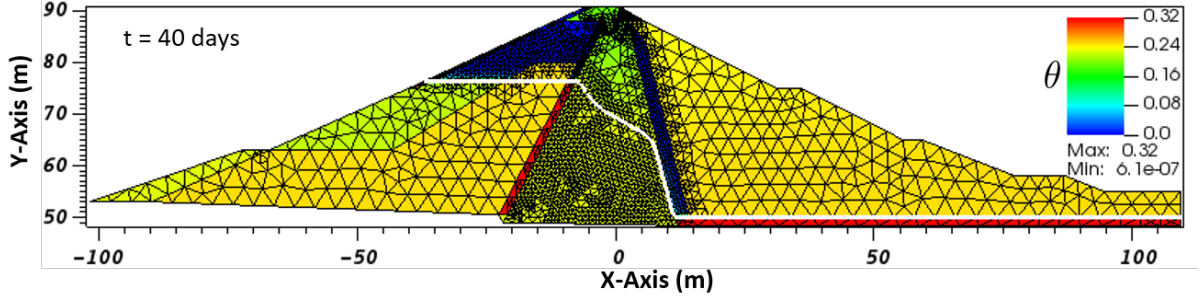
with the hydraulic diffusivity $D(\theta) = \mathbb{K}(\theta) \frac{d\psi(\theta)}{d\theta}$ [$L^2 \cdot T^{-1}$].

The Péclet number can therefore be defined as:

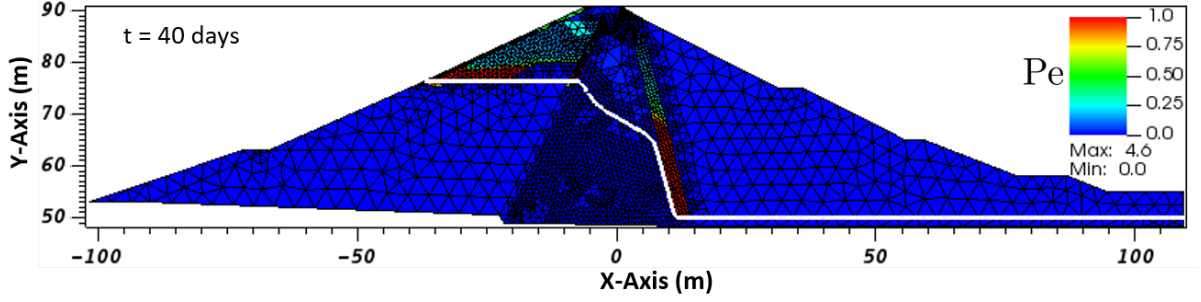
$$Pe = \frac{\mathbb{K}(\theta)L}{D(\theta)\theta} = \frac{C(\theta)L}{\theta}, \quad (50)$$

with the capillary capacity $C = \frac{d\theta(\psi)}{d\psi}$ [L^{-1}] and L the characteristic linear dimension assimilated to an element size h_E . High Péclet numbers are clearly reached in the sharp-gradient areas in Fig. 15, with m1-, m2- and m3-materials (i.e. drains, rip-rap and upstream shell) showing relatively high Péclet numbers, from 1 to more than 5. Consequently, water table is not straight anymore and a delay in elevation is observed upstream, see Fig. 13.

425



(a) Distribution of water content at $t = 40$ days



(b) Distribution of Péclet number at $t = 40$ days

Figure 15: Heterogeneity and nonlinear varying diffusivity highlighted respectively by water content and Péclet number for La Verne dam simulation with the reference simulation.

In order to overcome these limitations, an additional ad-hoc configuration, named *augmented* simulation, has been implemented. This one does not use WDG framework and other difference lies in the mesh and tolerances for nonlinear convergence criterion. Finer discretization is allowed in permeable material that is to say the m1-, m2- and m3-materials. The mesh is also refined around water table and both for the gradient-based and estimation-based error indicators. Instead of the reference simulation, 4-order BDF is employed and hydraulic properties are relaxed with a numerical minimal value to avoid complete degeneracy. The *augmented* computation allowed to eliminate spurious oscillations from the solution thanks to a more refined mesh, which explains why WDG method is not needed. As the mesh is extremely refined, the *augmented* simulation takes approximately four times longer to compute than the reference simulation.

The simulation of La Verne dam filling shows many difficult points which lead to two unwanted effects. The first one is the development of non-physical oscillations around steep wetting fronts associated with nonlinear varying diffusivity which affect solution accuracy. The other one is nonlinear convergence possible only with very small time steps so that the calculation duration is high. These challenges illustrate numerical issues of Richards' equation for heterogeneous media with high-varying diffusivity. The improvements offered by the *augmented* simulation support the idea that a series of heuristic tools (threshold values, maximum refinement level, refinement frequency, adaptive time steps) should be investigated to improve accuracy while maintaining cost-effectiveness.

6 Conclusion

In this work, a new strategy has been formulated for the solution of Richards' equation on the basis of discontinuous Galerkin method and adaptive mesh refinement. The approximation can

reach high-order both in space and time. Issues outlined in the introduction have been tackled and further discussed throughout the paper so the following concluding remarks can be drawn:

- The seepage boundary condition is directly incorporated into the DG weak formulation which makes its treatment natural and simple.
- The adaptive time stepping allows the nonlinear iterative solver to converge giving robustness.
- Mesh adaptation is employed to monitor spatial errors of the Richards' equation by capturing the moving wetting fronts thanks to an *a posteriori* error indicator.
- The adaptive mesh refinement is based on a block structure to surround large regions where wetting fronts move aiming to save computational time by avoiding systematic refinement. It also prepares a future parallelization.
- Oscillations in sharp wetting fronts of Richards' equation have been interpreted within the context of convection-diffusion equation. Wetting fronts are considered as internal layers due to the nonlinear varying, and possibly vanishing, diffusivity as well as material heterogeneity and anisotropy. A local Péclet number is exhibited to highlight troublesome regions. A weighted discontinuous Galerkin method is used to allow for jumps in the solution which better approximate the sharp internal layers. Mesh adaptation and the weighted framework work in synergy to capture and resolve sharp wetting fronts through the proposed *a posteriori* error indicator.

The strategy leads to mass conservative, efficient and robust solution of Richards' equation. However, the method holds heuristic parameters so that questions remain open regarding the numerical analysis, the *hp*-decision making, the nonlinear convergence or the error balance. All these aspects have great potential of improvements and will be investigated in future studies to optimize the solving of Richards' equation.

Acknowledgement

The first author is partially supported by a grant from Provence-Alpes-Côte d'Azur region, France.

References

- [1] Thomas Altazin, Mehmet Ersoy, Frédéric Golay, Damien Sous, and Lyudmyla Yushchenko. Numerical investigation of BB-AMR scheme using entropy production as refinement criterion. *International Journal of Computational Fluid Dynamics*, 30(3):256–271, mar 2016.
- [2] Peter Bastian. A fully-coupled discontinuous Galerkin method for two-phase flow in porous media with discontinuous capillary pressure. *Computational Geosciences*, 18(5):779–796, jul 2014.
- [3] Luca Bergamaschi and Mario Putti. Mixed finite elements and Newton-type linearizations for the solution of Richards' equation. *International Journal for Numerical Methods in Engineering*, 45(8):1025–1046, jul 1999.
- [4] Stéphane Bonelli, Frédéric Golay, and Olivier Débordes. Résolution auto-adaptative par éléments finis de problèmes de diffusion fortement non linéaires. *Revue Européenne des Éléments Finis*, 2(4):495–515, jan 1993.

- [5] N. T. Burdine. Relative Permeability Calculations From Pore Size Distribution Data. *Journal of Petroleum Technology*, 5(03):71–78, mar 1953.
- [6] Erik Burman and Paolo Zunino. A Domain Decomposition Method Based on Weighted Interior Penalties for Advection-Diffusion-Reaction Problems. *SIAM Journal on Numerical Analysis*, 44(4):1612–1638, jan 2006.
- [7] Michael A. Celia, Efthimios T. Bouloutas, and Rebecca L. Zarba. A general mass-conservative numerical solution for the unsaturated flow equation. *Water Resources Research*, 26(7):1483–1496, July 1990.
- [8] J.-B. Clément, F. Golay, M. Ersoy, and D. Sous. Adaptive Discontinuous Galerkin Method for Richards Equation. In *Topical Problems of Fluid Mechanics 2020*. Institute of Thermomechanics, AS CR, v.v.i., 2020.
- [9] T. Coupez and E. Hachem. Solution of high-Reynolds incompressible flow with stabilized finite element and adaptive anisotropic meshing. *Computer Methods in Applied Mechanics and Engineering*, 267:65–85, dec 2013.
- [10] Daniele A. Di Pietro, Alexandre Ern, and Jean-Luc Guermond. Discontinuous Galerkin Methods for Anisotropic Semidefinite Diffusion with Advection. *SIAM Journal on Numerical Analysis*, 46(2):805–831, jan 2008.
- [11] Vít Dolejší and Miloslav Feistauer. *Discontinuous Galerkin Method*. Springer International Publishing, 2015.
- [12] Vít Dolejší, Michal Kuraz, and Pavel Solin. Adaptive higher-order space-time discontinuous Galerkin method for the computer simulation of variably-saturated porous media flows. *Applied Mathematical Modelling*, 72:276–305, aug 2019.
- [13] Vít Dolejší and Miloslav Vlasák. Analysis of a BDF–DGFE scheme for nonlinear convection–diffusion problems. *Numerische Mathematik*, 110(4):405–447, sep 2008.
- [14] Yekaterina Epshteyn and Béatrice Rivière. Estimation of penalty parameters for symmetric interior penalty Galerkin methods. *Journal of Computational and Applied Mathematics*, 206(2):843–872, sep 2007.
- [15] A. Ern, A. F. Stephansen, and P. Zunino. A discontinuous Galerkin method with weighted averages for advection-diffusion equations with locally small and anisotropic diffusivity. *IMA Journal of Numerical Analysis*, 29(2):235–256, apr 2008.
- [16] Alexandre Ern and Jennifer Proft. Multi-algorithmic methods for coupled hyperbolic-parabolic problems. *International Journal of Numerical Analysis and Modeling*, 3(1):94–114, 2006.
- [17] Mehmet Ersoy, Frédéric Golay, and Lyudmyla Yushchenko. Adaptive multiscale scheme based on numerical density of entropy production for conservation laws. *Open Mathematics*, 11(8), jan 2013.
- [18] Matthew W. Farthing and Fred L. Ogden. Numerical Solution of Richards’ Equation: A Review of Advances and Challenges. *Soil Science Society of America Journal*, 81(6):1257–1269, 2017.

- [19] J. M. Fleureau and J. J. Fry. Validation des modèles de couplage sur ouvrages réels. Technical report, Ministère de la Recherche et de la Technologie/CNRS. Rapport Scientifique du GRECO "Géomatériaux", 1991.
- [20] Daniel Fuster, Gilou Agbaglah, Christophe Josserand, Stéphane Popinet, and Stéphane Zaleski. Numerical simulation of droplets, bubbles and waves: state of the art. *Fluid Dynamics Research*, 41(6):065001, dec 2009.
- [21] W. R. Gardner. Some Steady-State Solutions of the Unsaturated Moisture Flow Equation with Application to Evaporation from a Water Table. *Soil Science*, 85(4):228–232, apr 1958.
- [22] Paul Houston, Dominik Schötzau, and Thomas P. Wihler. Energy Norm A Posteriori Error Estimation of hp-Adaptive Discontinuous Galerkin Methods for Elliptic Problems. *Mathematical Models and Methods in Applied Sciences*, 17(01):33–62, jan 2007.
- [23] S. Irmay. On the hydraulic conductivity of unsaturated soils. *Transactions, American Geophysical Union*, 35(3):463, 1954.
- [24] W. Klieber and B. Rivière. Adaptive simulations of two-phase flow by discontinuous Galerkin methods. *Computer Methods in Applied Mechanics and Engineering*, 196(1-3):404–419, dec 2006.
- [25] F. Lehmann and Ph. Ackerer. Comparison of Iterative Methods for Improved Solutions of the Fluid Flow Equation in Partially Saturated Porous Media. *Transport in Porous Media*, 31(3):275–292, 1998.
- [26] H. Li, M. W. Farthing, C. N. Dawson, and C. T. Miller. Local discontinuous Galerkin approximations to Richards’ equation. *Advances in Water Resources*, 30(3):555–575, mar 2007.
- [27] H. Li, M. W. Farthing, and C. T. Miller. Adaptive local discontinuous Galerkin approximation to Richards’ equation. *Advances in Water Resources*, 30(9):1883–1901, sep 2007.
- [28] Florian List and Florin A. Radu. A study on iterative methods for solving Richards’ equation. *Computational Geosciences*, 20(2):341–353, mar 2016.
- [29] Frank Losasso, Frédéric Gibou, and Ron Fedkiw. Simulating water and smoke with an octree data structure. *ACM Transactions on Graphics*, 23(3):457, aug 2004.
- [30] Gianmarco Manzini and Stefano Ferraris. Mass-conservative finite volume methods on 2-D unstructured grids for the Richards’ equation. *Advances in Water Resources*, 27(12):1199–1215, dec 2004.
- [31] J. M. Melenk and B. I. Wohlmuth. On residual-based a posteriori error estimation in hp-FEM. *Advances in Computational Mathematics*, 15(1/4):311–331, 2001.
- [32] Cass T. Miller, Chandra Abhishek, and Matthew W. Farthing. A spatially and temporally adaptive solution of Richards’ equation. *Advances in Water Resources*, 29(4):525–545, apr 2006.
- [33] Chohong Min and Frédéric Gibou. A second order accurate level set method on non-graded adaptive cartesian grids. *Journal of Computational Physics*, 225(1):300–321, jul 2007.

- [34] Yechezkel Mualem. A new model for predicting the hydraulic conductivity of unsaturated porous media. *Water Resources Research*, 12(3):513–522, jun 1976.
- [35] Claudio Paniconi and Mario Putti. A comparison of Picard and Newton iteration in the numerical solution of multidimensional variably saturated flow problems. *Water Resources Research*, 30(12):3357–3374, December 1994.
- [36] D. J. Polmann, E. G. Vomvoris, D. McLaughlin, E. M. Hammick, and L. W. Gelhar. Application of Stochastic Methods to the Simulation of Large-scale Unsaturated Flow and Transport, 1988.
- [37] J. Proft and B. Rivière. Analytical and numerical study of diffusive fluxes for transport equations with near-degenerate coefficients. Technical Report TR-MATH 06-07, University of Pittsburgh, 2006.
- [38] J. Proft and B. Rivière. Discontinuous Galerkin methods for convection-diffusion equations with varying and vanishing diffusivity. *International Journal of Numerical Analysis and Modeling*, 6(4):533–561, 2009.
- [39] Béatrice Rivière. *Discontinuous Galerkin Methods for Solving Elliptic and Parabolic Equations*. Society for Industrial and Applied Mathematics, jan 2008.
- [40] Dominik Schötzau and Liang Zhu. A robust a-posteriori error estimator for discontinuous Galerkin methods for convection–diffusion equations. *Applied Numerical Mathematics*, 59(9):2236–2255, September 2009.
- [41] C. Scudeler, C. Paniconi, D. Pasetto, and M. Putti. Examination of the seepage face boundary condition in subsurface and coupled surface/subsurface hydrological models. *Water Resources Research*, 53(3):1799–1819, mar 2017.
- [42] Endre Süli and David F. Mayers. *An Introduction to Numerical Analysis*. Cambridge University Press, aug 2003.
- [43] P. Sochala, A. Ern, and S. Piperno. Mass conservative BDF-discontinuous Galerkin/explicit finite volume schemes for coupling subsurface and overland flows. *Computer Methods in Applied Mechanics and Engineering*, 198(27-29):2122–2136, may 2009.
- [44] Pierre Sochala. *Méthodes numériques pour les écoulements souterrains et couplage avec le ruissellement*. PhD thesis, École Nationale des Ponts et Chaussées, 2008.
- [45] Pavel Solin and Michal Kuraz. Solving the nonstationary Richards equation with adaptive hp-FEM. *Advances in Water Resources*, 34(9):1062–1081, sep 2011.
- [46] Adam Szymkiewicz. *Modelling Water Flow in Unsaturated Porous Media*. Springer Berlin Heidelberg, 2013.
- [47] R. Brad Thoms, Richard L. Johnson, and Richard W. Healy. User’s guide to the Variably Saturated Flow (VSF) process to MODFLOW, 2006.
- [48] F. T. Tracy. Clean two- and three-dimensional analytical solutions of Richards’ equation for testing numerical solvers. *Water Resources Research*, 42(8), aug 2006.
- [49] F. T. Tracy. Three-dimensional analytical solutions of Richards’ equation for a box-shaped soil sample with piecewise-constant head boundary conditions on the top. *Journal of Hydrology*, 336(3-4):391–400, apr 2007.

- 610 [50] F. T. Tracy. Testing Computational Algorithms for Unsaturated Flow. *The Open Hydrology Journal*, 4(1):227–235, mar 2010.
- [51] Georges Vachaud and Jean-Louis Thony. Hysteresis During Infiltration and Redistribution in a Soil Column at Different Initial Water Contents. *Water Resources Research*, 7(1):111–127, feb 1971.
- 615 [52] M. Th. van Genuchten. A Closed-form Equation for Predicting the Hydraulic Conductivity of Unsaturated Soils. *Soil Science Society of America Journal*, 44(5):892–898, sep 1980.
- [53] R. Verfürth. A posteriori error estimates for finite element discretizations of the heat equation. *CALCOLO*, 40(3):195–212, dec 2003.
- [54] Rüdiger Verfürth. A posteriori error estimates for non-linear parabolic equations. Technical Report report 361, Fakultät für mathematik, Ruhr-Universität, Bochum, D-44780 Bochum, December 2004.
- 620 [55] Rüdiger Verfürth. A posteriori error estimates for nonlinear problems: $L^r(0, T; W^{1,p}(\Omega))$ -error estimates for finite element discretizations of parabolic equations. *Numerical Methods for Partial Differential Equations*, 14(4):487–518, 1998.
- 625 [56] Rüdiger Verfürth. *A Posteriori Error Estimation Techniques for Finite Element Methods*. Oxford University Press, apr 2013.
- [57] Yuanyuan Zha, Jinzhong Yang, Jicai Zeng, Chak-Hau M. Tso, Wenzhi Zeng, and Liangsheng Shi. Review of numerical solution of Richardson–Richards equation for variably saturated flow in soils. *Wiley Interdisciplinary Reviews: Water*, 6(5), jun 2019.
- 630 [58] L. Zhu and D. Schotzau. A robust a posteriori error estimate for hp-adaptive DG methods for convection-diffusion equations. *IMA Journal of Numerical Analysis*, 31(3):971–1005, apr 2010.